

Stress-strain hysteresis during hydrostatic loading of porous rocks

Alvin T. Biyoghé¹, Yves M. Leroy^{*1}, Lucas Pimienta², and Robert W. Zimmerman¹

¹Department of Earth Science and Engineering, Imperial College London, UK,

²Laboratoire Fluides Complexes et leurs Réservoirs (UMR 5150), Université de Pau et des Pays de l'Adour, France

January 9, 2024

Abstract

A micro-mechanical model is proposed to predict the stress-strain hysteresis during the cyclic hydrostatic loading of fluid-saturated rocks under drained or undrained conditions. A spherical pore is surrounded by a cracked shell where local deviatoric stress develops despite the remote hydrostatic loading. The effective properties of the material composing the shell are constructed with the crack non-interactive scheme and the overall properties thanks to the spherical assemblage approach. The fluid pressure in both drained and undrained conditions is assumed uniform throughout the assemblage. A new analytical solution is proposed assuming all cracks to be closed and slipping either forwardly or reversely. It is shown with numerical simulations for drained conditions that this assumption is indeed respected for sufficiently small crack friction angles. However, for reasonable friction values, the closed cracks during the unloading phase could slip in either direction: reversely close to the pore and still forwardly away from the pore. Moreover, at critical radii, the slip could occur in either direction depending on their orientation. A similar micro-structural response is observed for undrained conditions, although the remote confining stress required to close the cracks is much larger. The model's predictions compare favorably with recent experimental data on dry sandstones and carbonates presented in a study of the strain amplitude influence on the transition between static and dynamic properties. The crack density and matrix elasticity modulus are sufficient fitting parameters to accurately predict the hysteresis loops, especially for porosity levels above 10%.

Keywords— porous media; frictional cracks; spherical assemblage; hydrostatic loading; hysteresis.

Table (1) The list of variables and parameters with their definition.

Symbol	Definition
	Geometry and field variables
R_P, R_S V_P, V_S, V_A, V_{SP} ϕ $(\underline{e}_r, \underline{e}_\varphi, \underline{e}_\theta)$ $\underline{\sigma}, (\sigma_r, \sigma_\varphi, \sigma_\theta)$ P $\underline{\epsilon}, (\epsilon_r, \epsilon_\varphi, \epsilon_\theta)$ $u(r)$ r, r'	pore and shell external radius current pore, shell, assemblage and specimen volumes initial assemblage porosity due to pore only spherical coordinates basis stress tensor and spherical components function of radial position hydrostatic stress, one third trace of $\underline{\sigma}$ strain tensor and spherical components function of radial position radial displacement function of radial position r radial position in shell, normalised by R_S
	Fluid
p_f κ_f V_f V_{fS} V_D, ϕ_D \mathcal{V}_f	fluid pressure fluid bulk modulus current total fluid volumes fluid content within shell, matrix and cracks contributions dead volume & equivalent porosity (divided by initial specimen volume) total fluid volume in specimen and dead volume
	Matrix composing the shell
κ, E, G α ν R_{pM} ϕ_M \mathbb{C}	bulk and shear elasticity modulus Biot's coefficient Poisson's ratio storage coefficient at constant deformation initial matrix porosity isotropic compliance fourth-order tensor
	Cracks within the shell
c ϕ_C l n $\underline{n}, \underline{p}, \underline{m}$ s \underline{T} σ_n $\underline{\tau}, \tau$ $\underline{\omega}$ $\underline{b}, \underline{b}_n, \underline{b}_t$ γ, \underline{B} φ, μ σ_C ζ (β, β') V_{fC} ϵ_{vC}	uniform crack density spherical distribution initial crack porosity crack radius no of cracks in a matrix representative volume V unit vectors normal to, orienting slip on the crack plane and defining the slip rate direction scalar equal to $\underline{m} \cdot \underline{p} = \pm 1$, positive for forward and negative for reverse slip. stress vector acting on the crack normal stress resolved shear stress vector and its norm backstress for kinematic hardening criterion displacement jump, normal and tangent components, across the crack surfaces crack compliance scalar and tensor friction angle and coefficient closing stress initial crack aspect ratio $\frac{\gamma}{2l}\sigma_C(1 - \nu/2)$ polar angles orienting the cracks normal fluid content within the cracks crack volume, function of radial position
	Effective properties
θ, θ^P σ_H κ^*, G^* α^* $\bar{\kappa}, \bar{\kappa}_u$ \bar{G} $\bar{\alpha}$ S \bar{v}, \bar{v}^P	assemblage volumetric strain and plastic part remote, hydrostatic stress function of time REV effective bulk & shear modulus for shell material REV equivalent Biot coefficient for shell material drained and undrained effective bulk modulus for assemblage spherical assemblage shear modulus effective Biot's coefficient for assemblage effective Skempton coefficient for assemblage assemblage pore volume fraction, and plastic part

21 Contents

22	1 Introduction	4
23	2 Problem description	4
24	2.1 The shell material as a homogenized medium	5
25	2.2 The fluid pressure	7
26	2.3 Effective properties via the spherical assemblage	8
27	2.3.1 Structure of the constitutive relations at the assemblage scale	9
28	2.3.2 Numerical solution	10
29	2.3.3 Analytical solutions for drained conditions	10
30	2.3.4 Analytical solution for undrained regime	10
31	3 Predictions of the model	11
32	3.1 Effect of crack parameters on the bulk modulus, drained conditions	11
33	3.2 Crack's response around the cavity, drained conditions.	13
34	3.3 Cyclic response with undrained conditions	15
35	4 Application to hydrostatic compression of dry specimens	16
36	5 Conclusion	19
37	A Elasticity solution	21
38	B Effective properties of an elastic medium with an isotropic distribution of open, circular cracks	21
39	C Finite-element solution	22
40	D Numerical algorithm for cracks aperture update	23
41	E Numerical algorithm for frictional cracks update	24
42	F Kinematic hardening	24
43	F.1 Kinematic hardening and fracture mechanics	25
44	F.2 A single family with azimuthal symmetry	25
45	G Spherical Assembly effective properties for slipping cracks	27

1 Introduction

There are at least two motivations for conducting laboratory hydrostatic loading tests, both under dry and saturated conditions, to estimate the elastic properties of rocks. The first motivation stems from the simplicity of the procedure, which leads to low experiment costs, especially under dry conditions. In the energy industry, this method connects variations in wave velocity with changes in fluid pressure, contributing to 4D seismic interpretations used for reservoir monitoring (Vasquez et al. [2019]). The second motivation stems from recent experimental advancements in the frequency and amplitude dependence of elastic properties to link the static and dynamic elastic properties (Pimienta et al. [2015]). However, this hydrostatic test presents some challenges. For instance, in static loading tests, different bulk modulus values are measured at various stages of the loading cycle. Moreover, the hysteresis between the loading and unloading stages is evidence of inelastic behavior despite the lack of any macroscopic deviatoric stress (Chapman et al. [2023], Wang et al. [2021], Jizba and Nur [1990], Martin III and Haupt [1994]). Our interest in this contribution is to propose a micro-structural model justifying the cause of hysteresis and predicting the hysteresis loop in hydrostatic tests.

The presence of cracks has long been identified as the leading cause of hysteresis in compression tests (Walsh [1965], Pimienta et al. [2015], Borgomano et al. [2017]). The matching between experiments and theoretical predictions of this hysteresis for uni-axial loading is now established (e.g. David et al. [2012]) but remains open for hydrostatic loading. Local deviatoric stress is needed to cause the cracks to slip and trigger hysteresis. It is for this reason that the model problem of a spherical pore inside a spherical cracked shell is proposed to generate the local deviatoric stress responsible for crack slip. The distributed cracks, once closed and slipping, reduce the local shear modulus and thus affect the effective bulk modulus of the assemblage. Despite the absence of crack propagation or interaction, this influence results in a hysteretic evolution of the effective bulk modulus of the assemblage.

Several elements are necessary to construct this model problem and are now reviewed. For the cracked shell, a first homogenization is considered to estimate its local effective properties, following the simple scheme for non-interactive penny-shaped cracks of Kachanov [1982]. This first homogenization supposes that the micro-cracks have the same dimensions, internal friction, and an isotropic distribution. In addition, to downplay the non-consideration of crack interaction, the value of the crack density is purposely exaggerated. Using these same hypotheses, Aleshin and Van Den Abeele [2007] and David et al. [2012] have reproduced the hysteresis in Young's modulus of micro-cracked rocks under cyclic uniaxial loading. The quality of their results was a motivation for using Kachanov's scheme, among other micro-mechanics models (Christensen [1990]), to predict the hysteresis of rocks under hydrostatic cyclic loading.

The second homogenization concerns the spherical cracked shell and the fluid-filled pore in interaction with the remote homogeneous media. It follows the work of Hashin [1962] and is referred to as the spherical assemblage. This approach has received considerable attention in the literature and, for example, could be generalized to an arbitrary number of layers [Hervé and Zaoui, 1993] or include interface conditions [Benveniste, 1985]. Closer to our application, Pan et al. [1996] included a cracked layer in the spherical assemblage and used the dilute concentration method to estimate the effective properties. They only accounted for the effect of the crack's compliance as the disturbing factor to linear elasticity. No composite sphere assemblage model containing frictional cracks has been proposed so far, at least to the authors' knowledge. The proposed model includes friction and accounts for the changes in the pore fluid pressure and volume (a dead fluid volume is also included) in drained or undrained conditions.

The contents of this contribution are as follows. Section 2 pertains to the presentation of the model problem, including the first homogenization scheme to define the shell material properties, the evolution of the fluid pressure for undrained conditions, and the expected structure of the poro-elasto-plastic constitutive response at the assemblage scale. Rice [1977]'s argument is evoked to suggest that the same Biot's coefficient enters the relation between stress, strain, and fluid pressure change as well as the relation between the pore volume fraction and the assemblage volume change. The analytical solutions for drained and undrained conditions are also presented for open cracks or for closed and sticking cracks. A new solution assuming all cracks slip is presented in Appendix G. Since the assumptions behind these analytical solutions are not always valid, a numerical solution based on the finite-element method is also proposed (Appendix C). The constitutive relations for open cracks and slipping cracks are discussed in Appendices D and E, respectively. The difficulty of the second algorithm for a Coulomb criterion is that the stress path is via the tip of the cone (yield surface) at crack closure, as shown in the Appendix F, which motivates the link between the fracture mechanics argument and the kinematic hardening plasticity model considered here. The hysteresis predicted by this model problem is presented in Section 3. The assemblage's response is found to compare well with the new analytical results for vanishing crack friction values only. It is shown, for reasonable frictional values, that the crack activation is indeed far from being homogeneous during the loading cycle, the major assumption of the analytical solution. Forward slip could still be activated within the shell material during the early unloading phase and is concurrent with the reverse slip afterward. Then, the impact of different crack parameters (crack closure stress, crack density, and friction) on the amount of hysteresis and the shape of the hysteresis loop is discussed. The predictions for undrained conditions are also presented. Section 4 proposes a set of numerical results matching the experimental data from Chapman et al. [2023] on the hydrostatic compression of different dry rock samples. The experimental hysteresis loops are well predicted while only using the crack density and the matrix elasticity modulus as fitting parameters.

2 Problem description

The model problem consists of a spherical assemblage consistent with the hydrostatic loading of interest and inspired by the numerous similar prototypes found in the literature since the early work of Hashin [1962]. The geometry of the micro-structural prototype is presented in Figure 1. It consists of a pore surrounded first by a shell and second by

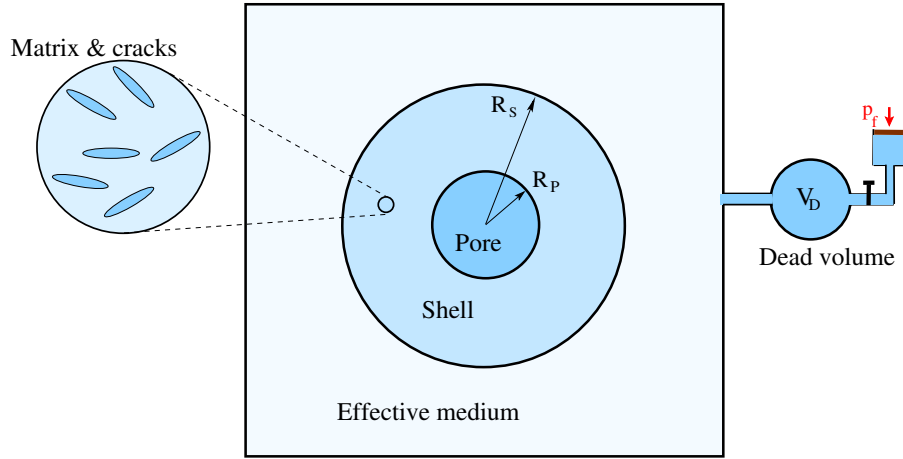


Figure (1) The specimen response is constructed with two homogenization schemes. The first scheme is for an isotropic distribution of cracks, represented symbolically in the inset, within a porous, fluid-saturated elastic matrix. The resulting material composes the shell of a spherical assemblage with a fluid-filled pore. The second homogenization scheme is for the interaction between the spherical assemblage and the effective medium, sustaining a homogeneous stress state. The fluid pressure is uniform over the specimen and equal to the pressure in the dead volume. The fluid mass is constant if the tap is closed. An open tap corresponds to a pressure-controlled experiment.

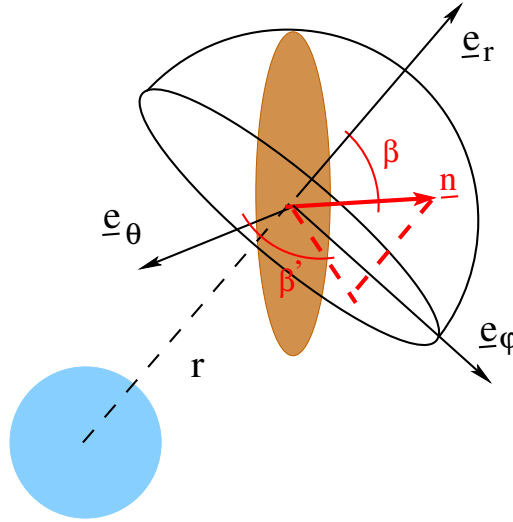


Figure (2) The distribution of cracks at an arbitrary material point within the shell at the distance r from the pore centre. Any crack in the isotropic distribution is oriented by its unit normal \underline{n} thanks to the two polar angles β and β' .

108 an infinite effective medium, sustaining a homogeneous, hydrostatic stress state. The ratio of the pore to the external
 109 shell radius is set to represent the poral porosity of the effective medium: $\phi = (R_P/R_S)^3$ (disregarding the secondary
 110 porosity of the shell matrix). The material composing the shell is a porous elastic and isotropic matrix with an isotropic
 111 distribution of initially open, penny-shaped cracks.

112 The constitutive relations are presented next in a rate form because of the non-linear evolution of internal parameters.
 113 However, no physical timescale is attached to the material or the fluid responses. The loading responsible for this evolution
 114 is initiated from hydrostatic conditions corresponding to the homogeneous stress state $-p_{f0}\underline{\underline{\delta}}$ within the assemblage and
 115 the fluid pressure p_{f0} . The deformation is set to zero at the initial conditions. Note that a zero in subscript defines
 116 the initial value of the highlighted quantity (at the exception of the various porosities) and that $\underline{\underline{\delta}}$ is the second-order
 117 identity tensor, underlined twice as all second-order tensors in what follows.

118 2.1 The shell material as a homogenized medium

119 The material composing the shell is a porous matrix with an isotropic distribution of cracks, and the whole is described
 120 via a homogenization scheme disregarding any crack interaction. The objective is to summarize this homogenization
 121 scheme presented by [Kachanov \[1982\]](#) and [Kachanov \[1992\]](#), to compute the fluid volume within the cracks, and to
 122 prepare the grounds for the interaction analysis with the pore.

123 Each material point within the shell is assumed to contain an isotropic distribution of circular micro-cracks with a
 124 dimensionless crack number nl^3/V in which n is the number of cracks of radius l contained in the REV of volume V .
 125 The strain rate over the representative elementary volume denoted $\underline{\underline{\dot{\epsilon}}}$ is the sum of the strain rates due to the matrix and
 126 to the cracks,

$$\underline{\dot{\epsilon}} = \mathbb{C} : (\underline{\dot{\sigma}} + \alpha \dot{p}_f \underline{\delta}) + \frac{c\pi}{2l} \int_{\mathcal{H}} \dot{b}(\underline{n}) \otimes \underline{n} + \underline{n} \otimes \dot{b}(\underline{n}) d\mathcal{H}, \quad (1)$$

in which \mathbb{C} is the isotropic matrix compliance fourth-order tensor, $\underline{\dot{\sigma}}$ is the stress rate tensor at the material point within the shell and α is Biot's coefficient. The integral in the right-hand side of (1) is over the hemisphere \mathcal{H} defining all possible orientations of the unit normal \underline{n} of the micro-cracks, Figure 2. Note the two polar angles β and β' in this Figure define the normal orientation and have the ranges $[0; \pi/2]$ and $[0, 2\pi]$, respectively. The definition of \mathcal{H} implies that the scalar c in (1) denotes the crack density spherical distribution $nl^3/(2\pi V)$ and is referred to as the crack density in what follows. For each crack orientation, there is an average displacement jump \underline{b} over the crack surfaces, which contributes to the definition of the strain rate in equation (1). The cracks are initially open, and the average displacement over the crack surfaces is then given by:

$$\underline{b} = \underline{B} \cdot (\underline{\dot{T}} + \dot{p}_f \underline{n}) \quad \text{with} \quad \underline{B} = \gamma (\underline{\delta} - \frac{\nu}{2} \underline{n} \otimes \underline{n}) \quad \text{and} \quad \gamma = \frac{32l}{3\pi E} \frac{1 - \nu^2}{2 - \nu}, \quad (2)$$

127 in terms of the second-order crack compliance tensor \underline{B} , the stress vector \underline{T} based on the stress at the material point
 128 within the shell and the crack compliance scalar γ function of E and ν , standing for the matrix elasticity modulus and
 129 Poisson's ratio, respectively. Note that it is the Terzaghi stress vector that is introduced in (2), whereas Biot effective
 130 stress is considered for the elastic matrix response in (1). Note also that the displacement jump is decomposed in
 131 tangential and normal components:

$$\underline{b} = \underline{b}_t + \underline{b}_n \quad \text{with} \quad \underline{b}_n = \gamma (1 - \frac{\nu}{2}) \underline{n} \otimes \underline{n} \cdot (\underline{\dot{T}} + \dot{p}_f \underline{n}) \quad \text{and} \quad \underline{b}_t = \gamma (\underline{\delta} - \underline{n} \otimes \underline{n}) \cdot (\underline{\dot{T}} + \dot{p}_f \underline{n}), \quad (3)$$

132 these relations to the effective stress vector being deduced from (2).

Cracks are fluid-saturated, and closure requires the effective normal component of the stress vector to be larger in magnitude than the closing stress σ_C , a positive scalar. This condition reads in terms of the total normal stress,

$$\sigma_n \leq -(\sigma_C + p_f) \quad \text{with} \quad \sigma_n = \underline{n} \otimes \underline{n} : \underline{\sigma}. \quad (4)$$

Combine the normal displacement relation in (3) and this closing condition to estimate the initial aspect ratio of the circular cracks, which is $\zeta = \frac{\gamma}{2l} \sigma_C (1 - \nu/2)$ (the displacement is divided by two to get the crack out-of-plane initial radius). This aspect ratio and its evolution during loading is essential to estimate the fluid volume contained in the cracks. In particular, the fluid volume within the cracks is computed as follows for initial conditions. Consider a hydrostatic loading and use equation (1) to determine the volume change for normal stress based on the closure criterion (4). The opposite value is the initial fluid volume in the cracks, which is referred to as the initial crack porosity:

$$\phi_C = \frac{32\pi}{3} \frac{\sigma_C}{E} (1 - \nu^2) c. \quad (5)$$

133 Once the crack is closed, only the tangential component of the average displacement discontinuity continues to evolve
 134 because of slip, and its rate is controlled by a Coulomb condition f_n . Slip is prevented if:

$$f_n \equiv |\underline{\tau} - \underline{\omega}_n| + \mu(\sigma_n + \sigma_C + p_f) < 0 \quad \text{with} \quad \underline{\tau} = (\underline{\delta} - \underline{n} \otimes \underline{n}) \cdot \underline{T}, \quad (6)$$

135 in which $\underline{\tau}$ is the resolved shear stress and $\underline{\omega}$ is referred to as the back-stress. This last terminology is proposed because of
 136 the analogy between criterion (6) and the structure of the kinematic hardening of plasticity [Prager, 1955], as mentioned
 137 by Andrieux et al. [1986]. The back-stress evolution is, however, different from what is constructed with a plasticity
 138 theory since it also evolves in the elastic range so that the criterion $f_n = 0$ at the transition between opening and
 139 closing. The consequence of this evolution up to crack closure is that at first inspection of the stick condition in (6), the
 140 stress point is precisely at the tip of the Coulomb cone in the stress space spanned by the resolved shear and effective
 141 normal stresses. The back-stress in the elastic domain is thus simply equal to the resolved shear stress $\underline{\tau}$, which, given
 142 its definition in (6) and the structure of the crack compliance tensor in (2) and (3), is interpreted as the tangential
 143 displacement jump \underline{b}_t divided by the compliance scalar γ : $\underline{\omega} = \underline{\tau} = (1/\gamma)\underline{b}_t$.

144 This relation between the tangential displacement jump and the back-stress is extended in a rate form if slip occurs:

$$\dot{\underline{b}}_t = \gamma \dot{\underline{\omega}}. \quad (7)$$

145 The back-stress rate $\dot{\underline{\omega}}$ is zero if the stick condition corresponding to $f_n < 0$ or $f_n = 0$ and $\dot{f}_n < 0$ is respected. Slip
 146 occurs if $f_n = 0$ and $\dot{f}_n = 0$, and the latter equation is the consistency condition leading to the back-stress rate evaluation
 147 done in two steps. First define the direction of the back-stress rate $\dot{\underline{\omega}}$ with:

$$\dot{\underline{\omega}} = \dot{\lambda} \underline{m} \quad \text{and} \quad \underline{m} = \frac{\underline{\tau} - \underline{\omega}}{|\underline{\tau} - \underline{\omega}|}, \quad (8)$$

in which \underline{m} is a unit vector and second, use the consistency condition to determine the rate of the yet unknown scalar $\dot{\lambda}$, where:

$$\dot{\lambda} = \underline{m} \cdot \dot{\underline{\tau}} + \mu(\dot{\sigma}_n + \dot{p}_f). \quad (9)$$

148 A simple application of this framework to understand the response of a single crack family with azimuthal symmetry is
 149 presented in Appendix F.

150 Further information is required to describe the fluid content at each material point composing the shell via what
 151 is classically called the pore volume fraction in the poro-mechanics literature [Rice and Cleary, 1976]. In the present
 152 setting, this variable corresponds to the fluid volume within the elastic matrix and the cracks normalized by the initial
 153 volume of the REV.

154 There is indeed a relation between the REV pore volume fraction rate of change \dot{v} with first the fluid pressure and
 155 second the local matrix volume change, the latter being the difference between the REV rate $\dot{\epsilon}_v$ and the volume change
 156 of the cracks $\dot{\epsilon}_{vC}$. In this study, such relation is proposed as if an energy potential was postulated [Rice, 1977], and
 157 consistently with equation (1):

$$\dot{v} = \alpha(\dot{\epsilon}_v - \dot{\epsilon}_{vC}) + R_{pM}\dot{p}_f + \dot{\epsilon}_{vC}, \quad (10)$$

with $\dot{\epsilon}_{vC} = \frac{c\pi\gamma}{l}(1 - \frac{\nu}{2}) \int_{\mathcal{H}_O} (\dot{\sigma}_n + \dot{p}_f) d\mathcal{H}$ and $R_{pM} = \frac{(1 - \alpha)(\alpha - \phi_M)}{\kappa}$.

158 The additional material constant R_{pM} is the storage coefficient at constant volumetric strain defined here in terms of
 159 Biot's coefficient, the bulk modulus κ and the initial porosity ϕ_M of the elastic, isotropic matrix material composing the
 160 shell. Note that the integral in equation (10) is restricted to the part of the hemisphere \mathcal{H}_O corresponding to open cracks
 161 and that the integrand was obtained from the normal part of the crack displacement jump defined in equation (3).

162 2.2 The fluid pressure

163 The fluid pressure during a test could either be controlled externally by a pump or vary because the total fluid mass is
 164 conserved. In Figure 1, the controlled pressure case corresponds to an open tap letting the fluid flow to or from a reservoir
 165 where the fluid level changes, ensuring that the pressure is at the desired value. If the tap is closed, the pressure varies
 166 because the fluid mass within the specimen and the dead volume are conserved. In both cases, the specimen permeability
 167 is assumed to be large enough or equivalently that the loading rate is slow enough so that the fluid pressure change is
 168 homogeneous over the whole fluid system. Consequently, these two cases correspond to locally drained conditions with
 169 controlled pressure or constant fluid mass. Nevertheless, they will be referred to as drained and undrained conditions in
 170 what follows having in mind the macro-scale response. This section aims to evaluate the pressure change during loading
 171 if the fluid mass is kept constant under undrained conditions.

172 The total fluid volume within the experimental system has contributions from the pore, the shell volume due to its
 173 porosity and the presence of cracks, and from the dead volume. The latter is constant in time, and the question is the
 174 evaluation of two earlier volume changes. First, consider the shell material and the pore volume fraction change of the
 175 REV is the integral through the loading of the expression in (10):

$$v = \frac{\alpha}{\kappa}[P + \alpha p_f + (1 - \alpha)p_{f0}] + R_{pM}(p_f - p_{f0}) + \epsilon_{vC}, \quad (11)$$

with $\epsilon_{vC} = \frac{c\pi\gamma}{l}(1 - \frac{\nu}{2}) \left(\int_{\mathcal{H}_O} (\sigma_n + p_f) d\mathcal{H} - \int_{\mathcal{H}_C} \sigma_C d\mathcal{H} \right)$,

176 in terms of the hydrostatic stress $P = \text{tr}(\underline{\sigma})/3$, a third of the stress tensor trace. This stress is introduced because the
 177 elastic part of the constitutive relation in (1) has been used to eliminate the elastic part of the REV strain rate in (10).
 178 The volume change due to the cracks ϵ_{vC} is defined in equation (11)b with two integrals. The first integral is over \mathcal{H}_O ,
 179 the part of the hemisphere corresponding to open cracks, and the second \mathcal{H}_C over the complementary part where the
 180 cracks are closed. The second integrand is based on the closure criterion (4). The two quadratures over the hemisphere
 181 are now included following the techniques presented in Appendices B and D:

$$\epsilon_{vC} = \frac{c\pi^2\gamma}{3l}(2 - \nu)((\sigma_r + p_f)(1 - \cos^3 \beta_c) + (\sigma_\theta + p_f)(2 - 3 \cos \beta_c + \cos^3 \beta_c) - 3\sigma_C \cos \beta_c), \quad (12)$$

182 with the introduction of β_c , the critical value of the first polar angle, which marks the limit of crack closure in the interval
 183 $[0; \pi/2]$ according to the condition (4).

The contribution of the REV to the shell material, equations (11) and (12), is now integrated over the shell domain
 to obtain the normalised shell fluid volume relative change

$$\frac{V_{fS} - V_{fS0}}{V_{S0}} = (R_{pM} + \frac{\alpha^2}{\kappa})(p_f - p_{f0}) + \frac{3\alpha}{\kappa(1 - \phi)} \int_{\phi^{1/3}}^1 (P + p_{f0}) r'^2 dr' + \frac{c\pi^2\gamma}{l} \frac{2 - \nu}{1 - \phi} \int_{\phi^{1/3}}^1 [(\sigma_r + p_f)(1 - \cos^3 \beta_c) + (\sigma_\theta + p_f)(2 - 3 \cos \beta_c + \cos^3 \beta_c) - 3\sigma_C \cos \beta_c] r'^2 dr \quad \text{with } V_{fS0} = V_{S0}(\phi_M + \phi_C), \quad (13)$$

184 with the normalisation $r' = r/R_S$ and noting that the angle β_c is now a function of the radial position. The volume V_{S0}
 185 is the initial volume of the outer shell of the assembly $4\pi(R_S^3 - R_P^3)/3$ and V_{fS0} the initial shell fluid volume, which is
 186 due to its matrix porosity ϕ_M and to the initial crack porosity ϕ_C , the second defined in equation (5)

The second contribution to the fluid volume of the spherical assembly is due to the pore:

$$V_P - V_{P0} = 3 \frac{u(R_P)}{R_P} V_{P0} \quad \text{with } V_{P0} = \frac{4\pi}{3} R_P^3, \quad (14)$$

187 expressed in terms of the radial displacement at the pore wall.

The current total fluid volume within the assemblage is then deduced from (13) times V_{S0} and (14). Divide this resulting scalar by the initial volume of the assemblage V_{A0} , multiply that by the initial volume of the specimen V_{SP0} , and add the volume of the dead volume V_D to obtain the total fluid content within the experimental system depicted in Figure 1. This global volume \mathcal{V}_f is now presented normalized by the initial specimen volume:

$$\frac{\mathcal{V}_f}{V_{SP0}} \equiv (V_P + V_{fS}) \frac{1}{V_{A0}} + \phi_D, \quad \text{with} \quad \phi_D = \frac{V_D}{V_{SP0}}, \quad (15)$$

introducing an apparent additional porosity ϕ_D defined as the dead volume divided by the initial volume of the specimen. The initial value of the normalized global volume in (15) is:

$$\frac{\mathcal{V}_{f0}}{V_{SP0}} = \phi + (\phi_M + \phi_C)(1 - \phi) + \phi_D, \quad (16)$$

having introduced the initial assemblage porosity ϕ , matrix porosity ϕ_M , and fracture porosity ϕ_C . The variation of the global fluid volume in equation (15) is:

$$\frac{\Delta \mathcal{V}_f}{V_{SP0}} = \frac{\Delta V_P}{V_{P0}} \phi + \frac{\Delta V_{fS}}{V_{S0}} (1 - \phi), \quad (17)$$

since the dead volume is constant throughout the loading and having introduced the symbol Δ to denote the variation of the various volumes from their initial conditions. This global fluid volume change, normalized by its initial value, is also related to the fluid pressure change and its bulk modulus κ_f so that, combining (16) and (17):

$$\frac{\Delta V_P}{V_{P0}} \phi + \frac{\Delta V_{fS}}{V_{S0}} (1 - \phi) = -\frac{p_f - p_{f0}}{\kappa_f} [\phi + (\phi_M + \phi_C)(1 - \phi) + \phi_D]. \quad (18)$$

188 The combination of the results in (18) with (14) and (13), after some simplifications, provide the equation for the fluid
189 pressure:

$$Y_p(p_f - p_{f0}) = Y_H \quad \text{with} \quad (19)$$

$$Y_p = -\left(\frac{\phi_D + \phi}{\kappa_f} + (1 - \phi)(R_{pM} + \frac{\alpha^2}{\kappa} + \frac{\phi_M + \phi_C}{\kappa_f}) + \frac{3c\pi^2\gamma}{l}(2 - \nu) \int_{\phi^{1/3}}^1 [1 - \cos \beta_c] r'^2 dr' \right)$$

$$\text{and} \quad Y_H = 3\phi \frac{u(R_P)}{R_P} + \int_{\phi^{1/3}}^1 \left[\frac{3\alpha}{\kappa}(P + p_{f0}) + \frac{c\pi^2\gamma}{l}(2 - \nu)[(\sigma_r + p_{f0})(1 - \cos^3 \beta_c) + (\sigma_\theta + p_{f0})(2 - 3\cos \beta_c + \cos^3 \beta_c) - 3\sigma_C \cos \beta_c] r'^2 dr' \right]$$

Two special cases are of interest, the first corresponding to a matrix with open cracks ($\beta_c = \pi/2$ at every radius r' in equation 19). The elasticity solution provided in Appendix A is then used to find the following relation between the remote stress and the pressure change

$$p_f - p_{f0} = S(\sigma_H - p_{f0}) \quad \text{with} \quad S = \frac{Z_H}{Z_p}, \quad (20)$$

$$Z_p = \frac{1}{\kappa_f} [\phi_D + \phi + (\phi_M + \phi_C)(1 - \phi)] + (R_{pM} + \frac{\alpha^2}{\kappa})(1 - \phi) + \frac{c\pi^2\gamma}{l}(2 - \nu)$$

$$+ \frac{\alpha\phi}{\kappa} - \phi \frac{1 - \alpha^*}{\kappa^*} + \frac{3\phi}{1 - \phi} \left(\frac{1}{3\kappa^*} + \frac{1}{4G^*} \right) \quad \text{and}$$

$$Z_H = \frac{3\phi}{1 - \phi} \left(\frac{1}{3\kappa^*} + \frac{1}{4G^*} \right) + \frac{\alpha}{\kappa} + \frac{c\pi^2\gamma}{l}(2 - \nu),$$

190 the definition of the triplet, $(\alpha^*, \kappa^*, G^*)$ being found in equation (45) in Appendix B. The second case of interest is if
191 all cracks are closed, although equation (20) should be applied to some reference stress conditions other than the initial
192 ones. For this second special case the same triplet equals the solid matrix value (α, κ, G) and the crack density c is set to
193 zero. In these two extreme cases, the relation in (20) is linear, as expected, showing that the loading through a pressure
194 change or the remote loading is proportional with a constant S , which could be interpreted as Skempton's coefficient. In
195 all intermediate cases, including slipping cracks, the general formula (19) has to be used, and the results will be based
196 on the numerical approach.

197 2.3 Effective properties via the spherical assemblage

198 The spherical assemblage presented in Figure 1 is now further discussed. The compressive stress within the effective
199 medium surrounding the sphere is isotropic with hydrostatic stress (one-third of the trace) equal to $-\sigma_H$. The interest
200 is to determine the effective properties of the porous medium ensuring stress continuity at the hollow sphere external
201 radius either by numerical or analytical means. The structure of the constitutive relations expected at the assemblage
202 level is first discussed before introducing the analytical and numerical solutions.

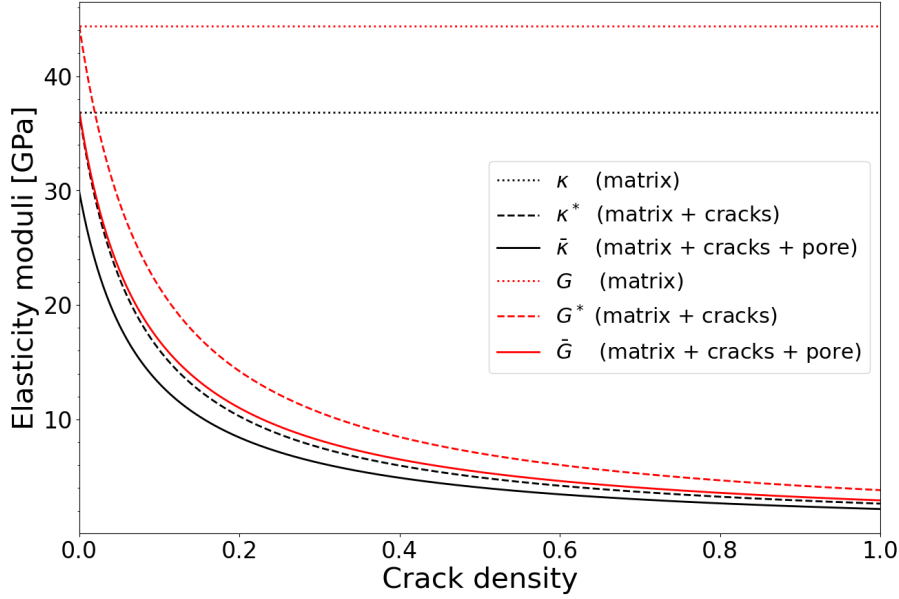


Figure (3) The influence of the crack density on the effective elastic properties of the matrix with cracks (κ^* , G^*) and of the spherical assemblage ($\bar{\kappa}$, \bar{G}). Predictions based on the analytical solutions assuming that all cracks are open and from Christensen [1990] for the assemblage effective shear modulus \bar{G} .

2.3.1 Structure of the constitutive relations at the assemblage scale

For drained tests, following Rice [1977], the energy rate of change of the spherical assemblage should be described by:

$$\dot{\mathcal{E}} = -\dot{\theta}\sigma_H + p_f\dot{v} - \langle F\dot{\xi} \rangle, \quad (21)$$

in which θ and \bar{v} are the volumetric deformation and the pore volume fraction of the assemblage, respectively. The scalar F stands for the collection of thermodynamic forces conjugate to the collection of internal variables ξ introduced in the section above to describe the crack response. The brackets $\langle \rangle$ in equation (21) denote the volume average over the assemblage. The thermodynamic forces are dependent on the local Terzaghi stress within the shell material so that it can be claimed that the volume average in equation (21) is only a function of the effective stress $-\sigma_H + p_f$ and its rate. This dependence on Terzaghi stress developed by Rice [1977] leads to the equality between the irreversible volume change and the irreversible fluid fraction rate:

$$\dot{\theta}^p = \dot{v}^p = -\mathbb{A}(\dot{\sigma}_H - \dot{p}_f), \quad (22)$$

an equality which is further extended here by stating that these two rates must be proportional to the remote effective stress rate, introducing a non-linear function \mathbb{A} of the remote effective stress and the collection of internal variables. This preliminary was necessary to introduce the rate form of the assemblage response under drained conditions, which reads:

$$\begin{aligned} \dot{\sigma}_H &= -\bar{\kappa}^e(\dot{\theta} - \dot{\theta}^p) + \bar{\alpha}^e\dot{p}_f, \\ \dot{v} - \dot{v}^p &= \bar{\alpha}^e(\dot{\theta} - \dot{\theta}^p) + \bar{R}_p^e\dot{p}_f, \end{aligned} \quad (23)$$

in which $\bar{\kappa}^e$, $\bar{\alpha}^e$ and \bar{R}_p^e are the elastic effective bulk modulus, the elastic Biot's coefficient and the elastic storage coefficient at constant volume change of the assemblage. This elastic bulk modulus contributes partly to the P wave velocity assuming a long wavelength compared to the radius of the assemblage. However, the interest here lies with the static estimate of the elastic properties with a sufficiently large strain increment so that the crack response is also involved. In other words, the linearisation of the non-linear properties developed above should provide the relevant properties. These static properties are obtained by combining (22) and (23):

$$\begin{aligned} \dot{\sigma}_H &= -\bar{\kappa}\dot{\theta} + \bar{\alpha}\dot{p}_f \quad \text{with} \quad \bar{\kappa} = \frac{\bar{\kappa}^e}{1 + \bar{\kappa}^e\mathbb{A}} \quad \text{and} \quad \bar{\alpha} = \frac{\bar{\alpha}^e + \bar{\kappa}^e\mathbb{A}}{1 + \bar{\kappa}^e\mathbb{A}}, \\ \dot{v} &= \bar{\alpha}\dot{\theta} + \bar{R}_p\dot{p}_f \quad \text{with} \quad \bar{R}_p = \bar{R}_p^e + (1 - \bar{\alpha}^e)^2 \frac{\mathbb{A}\bar{\kappa}^e}{\bar{\kappa}^e}. \end{aligned} \quad (24)$$

The interesting result is that despite the dissipation mechanisms, there is symmetry in the above set of equations. The same Biot's coefficient can be estimated by comparing the remote stress change and the fluid pressure change (at constant volume) or by relating fluid volume change and assemblage volume change (at constant fluid pressure). This finding is confirmed in Appendix G for the case where all cracks in the assemblage shell are closed and slipping. This finding also justifies our estimate of static Biot's coefficient by using the second equation in (23) in what follows. This practice, convenient from the numerical point of view, is at odds with the laboratory procedure.

For undrained tests, the two constitutive relations at the assemblage scale are first between the remote stress rate $\dot{\sigma}_H$ and the volumetric strain rate and second the definition of the evolution of the uniform pressure:

$$\dot{\sigma}_H = -\bar{\kappa}_u \dot{\theta} \quad \text{and} \quad p_f = p_{f_0} + \frac{Y_H}{Y_p}. \quad (25)$$

in which the two variables Y_H and Y_p , defined in equation (19), are function of the current value of the fluid pressure via the angle β_c and, more generally, of the state of stress within the assemblage. The bulk modulus is denoted $\bar{\kappa}_u$ as an undrained modulus since the fluid mass is conserved over the assemblage, including the dead volume.

2.3.2 Numerical solution

The solution for the model problem requires a numerical approach, which relies on the displacement-based finite-element method presented in Appendix C. The numerical algorithms to capture first the cracks aperture evolution and second the frictional deformation are found in Appendix D and E, respectively.

For the drained tests, two of the three effective properties, Biot's coefficient $\bar{\alpha}$, and the bulk modulus are deduced from the numerical solutions as follows. Time is discretised, and the volumetric deformation increment during the time increment Δt is $\Delta\theta = 3\Delta u(R_S)/R_S$ in terms of the radial displacement increment at the radius R_S . The effective bulk modulus $\bar{\kappa}$ during this increment for a constant fluid pressure test is then obtained by taking the ratio between the stress increment applied on the outer surface of the assemblage and the volumetric deformation increment. The fluid pressure being constant, Biot's coefficient $\bar{\alpha}$ is deduced from the second equation in (24) in which the pore volume fraction rate is interpreted as the fluid volume rate resulting from the contribution of the pore, the matrix, and the cracks, as defined in the previous section. The storage coefficient at constant volumetric strain is not computed but could be estimated with the following strategy: at any level of the applied load σ_H , first freeze the outer sphere radial displacement and thus the volumetric strain and second apply an incremental change in fluid pressure: the pore volume fraction of the assembly will then be modified providing the storage coefficient.

The numerical solution is coupled for the undrained tests since the fluid pressure changes over time. The solution strategy consists of a staggered scheme in which the fluid pressure is updated at the end of each time increment once a new equilibrium has been reached. The update is based on the solution of equation (19) which is obtained with a fixed-point method. The effective bulk modulus is still determined, as discussed above.

2.3.3 Analytical solutions for drained conditions

Analytical solutions are obtained for the assemblage effective properties in four instances, and three are grouped because the REV within the shell material is described in a rate form by the three parameters $(\alpha^*, \kappa^*, G^*)$ as for a poro-elastic, homogeneous material. This is the case, of course, for a shell material with completely closed cracks at any radial position around the pore, and in this instance, the set of moduli corresponds to the matrix properties. It is also the case of a matrix with all cracks being open for any radial position, and the corresponding moduli are presented in equation (45) developed in Appendix B. The third instance is if all cracks are closed and slipping with no friction, and the three moduli are defined by equation (79) constructed as a particular case in Appendix (G). The assembly response for these three cases is presented in the Appendix (A) and the effective properties then read:

$$\bar{\kappa} = \kappa^* \frac{1 - \phi}{1 + \phi \frac{3\kappa^*}{4G^*}}, \quad \bar{\alpha} = 1 - (1 - \alpha^*) \frac{\bar{\kappa}}{\kappa^*}, \quad (26)$$

There is a fourth analytical solution for the effective properties if all cracks are closed and slipping with a non-zero friction coefficient in forward or reverse slip (Appendix G). The effective properties are found in equation (78) and denoted $(\bar{\alpha}_s, \bar{\kappa}_s)$.

These analytical solutions are illustrated in Figure 3 constructed for a quartz matrix ($\kappa = 37 \text{ GPa}$, $\nu = 0.07$) and a pore porosity of 12.5%. The dotted, dashed and solid curves are the properties of the matrix, the REV (matrix+cracks) and of the assemblage, respectively. The red and black curves are for the shear and bulk moduli, respectively. Note that the shear modulus are based on the solution of Christensen and Lo [1979] and presented in Christensen [1990]. The assemblage properties for a zero density are smaller than the quartz values by 20 % and 30 % for the shear and the bulk modulus, respectively. A crack density of 20 % is enough for the drop to be by a factor of four to five from the matrix properties. These results show that the presence of the pore provides a minor part of the drop in both the bulk and shear modulus, which is dominated by the influence of crack density. One could tentatively use these results to forecast the evolution of the assemblage bulk modulus during a hydrostatic loading leading to the closure of the cracks: the bulk modulus could be increased by a factor of four to five.

2.3.4 Analytical solution for undrained regime

For a linear material with either all open or all closed cracks at any radius of the spherical assemblage, the effective bulk modulus has the following expression [Zimmerman, 2000]:

$$\bar{\kappa}_u = \frac{\bar{\kappa}}{1 - \bar{\alpha}S}, \quad (27)$$

having combined equation (20) with (24a) and $\bar{\kappa}$ and $\bar{\alpha}$ given in (26). This scalar $\bar{\kappa}_u$ is tentatively interpreted as the undrained bulk modulus of the spherical assemblage.

The analytical solutions just presented deserve further discussion, which will of great help in explaining the non-linear solutions presented next. Biot's coefficient and Skempton's coefficient, defined in equation (20), are presented

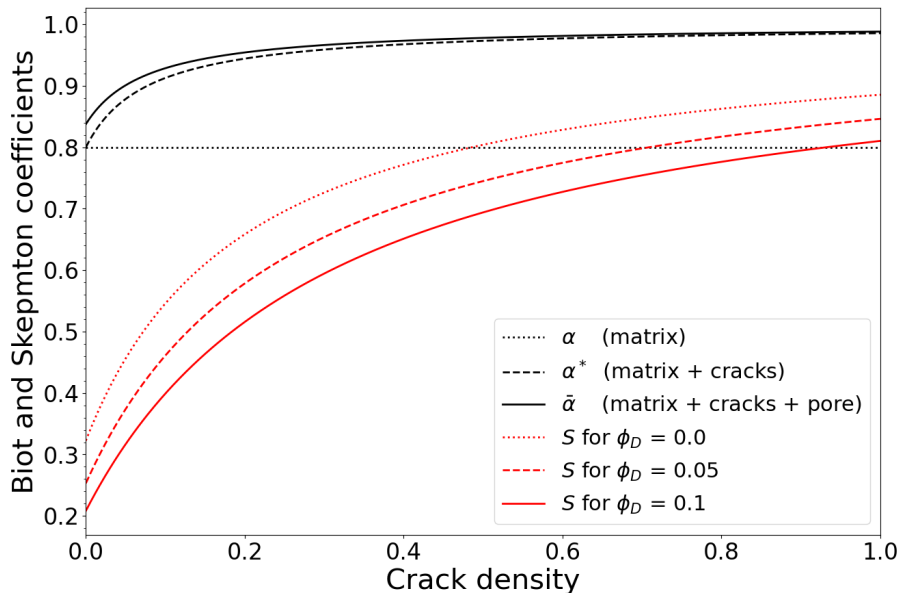


Figure (4) The influence of the crack density on the two effective Biot’s coefficients (the REV α^* and the assemblage $\bar{\alpha}$) and on the assemblage Skempton’s coefficient, for three values of the dead volume equivalent porosity. Predictions based on the analytical solutions assuming all cracks to be open.

in Figure 4 as a function of the crack density. The dotted horizontal line corresponds to the matrix Biot’s coefficient. The black dashed and solid curves depict the effective Biot’s coefficient of the REV and the assemblage, respectively. It does compare to the matrix value for a zero crack density and increases up to 20% with increasing crack density. The three red curves correspond to the variation of Skempton’s coefficient with the crack density for three values of the void porosity (ϕ_D is the volume of the dead volume divided by the specimen volume). There is a variation of the order of four as the crack density is increased to one. The presence of the dead volume leads to an underestimate of the true Skempton’s coefficient.

3 Predictions of the model

The influence of different crack parameters on the macroscopic bulk modulus during a cyclic hydrostatic test is analyzed first, followed by an analysis of the cracks’ behavior at the micro-scale. The pore fluid pressure ($p_f = 0.1$ MPa) is kept constant for drained simulations, and the porosity is set to $\phi = 12.5\%$. The confining pressure (σ_H) is increased from 0.1 MPa to 30 MPa (drained simulations) or 70 MPa (undrained simulations) and then decreased back to the initial value. The numerical predictions are compared with the analytical solutions if all cracks are closed and sticking or open (Appendix B) and if all cracks are slipping in forward or reverse mode (Appendix G).

3.1 Effect of crack parameters on the bulk modulus, drained conditions

To assess the impact of the three different crack parameters (μ , σ_C , and c) used in the model, we conducted multiple cyclic hydrostatic simulations. Each parameter was varied individually, while the other two and the pore fluid pressure were kept constant.

Figure 5a shows the evolution during a loading cycle of the bulk modulus as a function of confining pressure at $\mu = 0.6$, $c = 0.6$, and $\sigma_C = 5$ MPa (orange curve). The bulk modulus is bounded by two values. The lower bound (lower dashed black line) at $\kappa = 3.27$ GPa is the bulk modulus of the assemblage for open cracks. The upper bound (upper dashed line) is the bulk modulus, assuming all cracks are closed and sticking at $\kappa = 28.8$ GPa. The prediction matching perfectly with the lower bound is logical, as all cracks are initially open. During loading, cracks start closing slightly before the closure stress of 5 MPa. At a compression of 10 MPa, the bulk modulus is increased by approximately nine times, reaching an asymptote somewhat lower than the analytical solution for all cracks closed and sticking provided. Upon unloading, the prediction plateaus at the upper bound before decreasing back to the initial value of the bulk modulus, revealing the hysteresis effect and the crack’s dissipation. Figure 5a does not show the asymptotic solutions that assume all cracks slip in forward or reverse modes. These two asymptotes at 33.3 MPa and 14.3 MPa, not shown on the Figure, are off numerical predictions, indicating that some assumptions made for this analytical solution are not valid in this particular case.

Interestingly, this discrepancy disappears if the friction value of the crack is lowered close to zero (see the two dotted horizontal lines in Figure 5b). The predictions match at the end of loading and after the early unloading stage. Also, the friction coefficient doesn’t affect the early phase of loading and the final phase of unloading when the loading approaches the crack closure stress.

Figure 5c illustrates the impact of this closure stress. As it decreases, the closed loops shift towards the left. However,

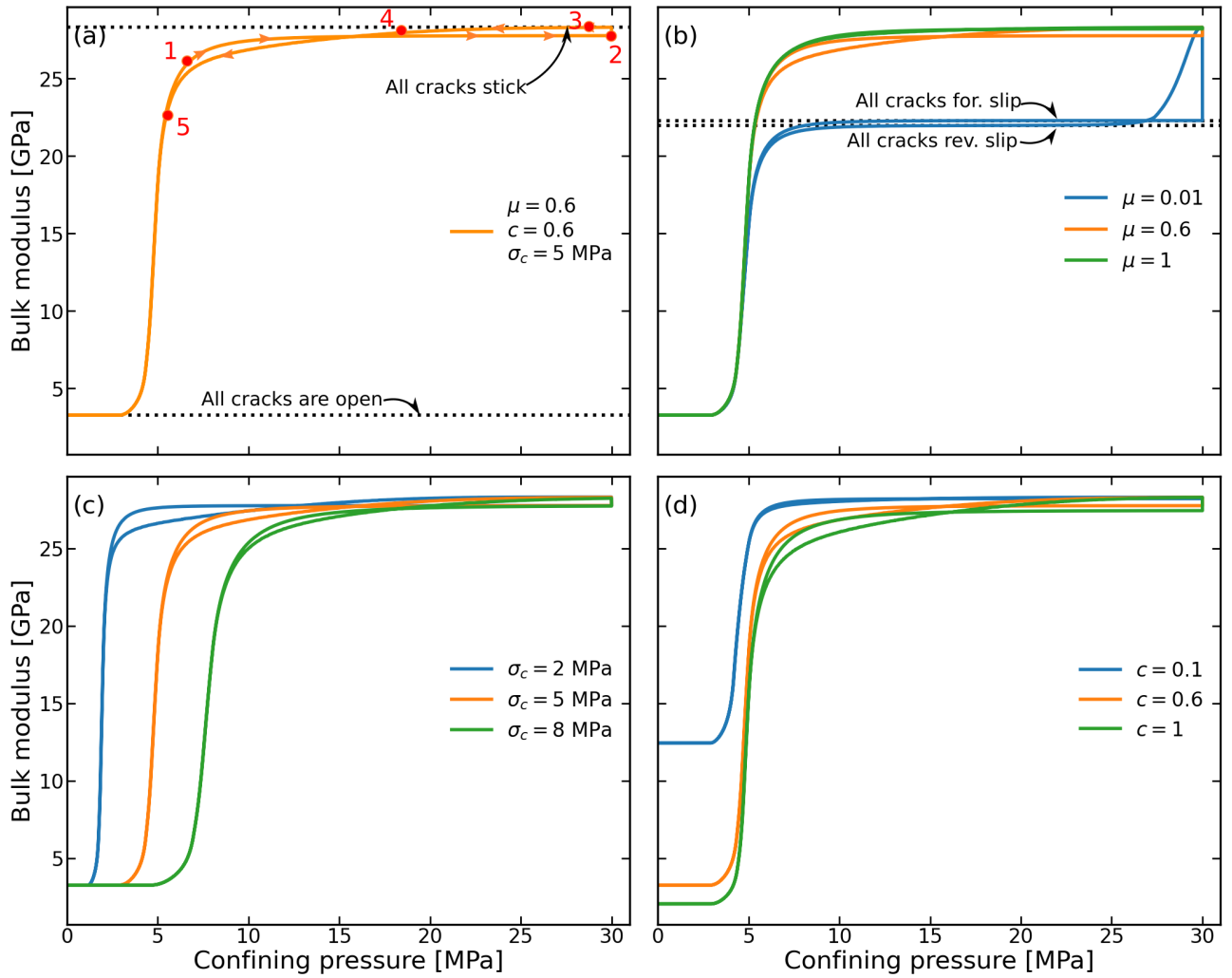


Figure (5) The cyclic evolution of the bulk modulus with the confining pressure, the reference simulation in (a). Influence of the friction coefficient, the closure stress, and the crack concentration, in (b), (c), and (d), respectively. Dotted lines are analytical solutions for cracks all open or closed, sticking or sliding in reverse or forward modes.

313 the minimum and maximum predictions remain unchanged by this parameter. These two values are highly sensitive to
 314 the crack concentration, shown in Figure 5d. Nevertheless, the crack concentration has little effect on the transition.

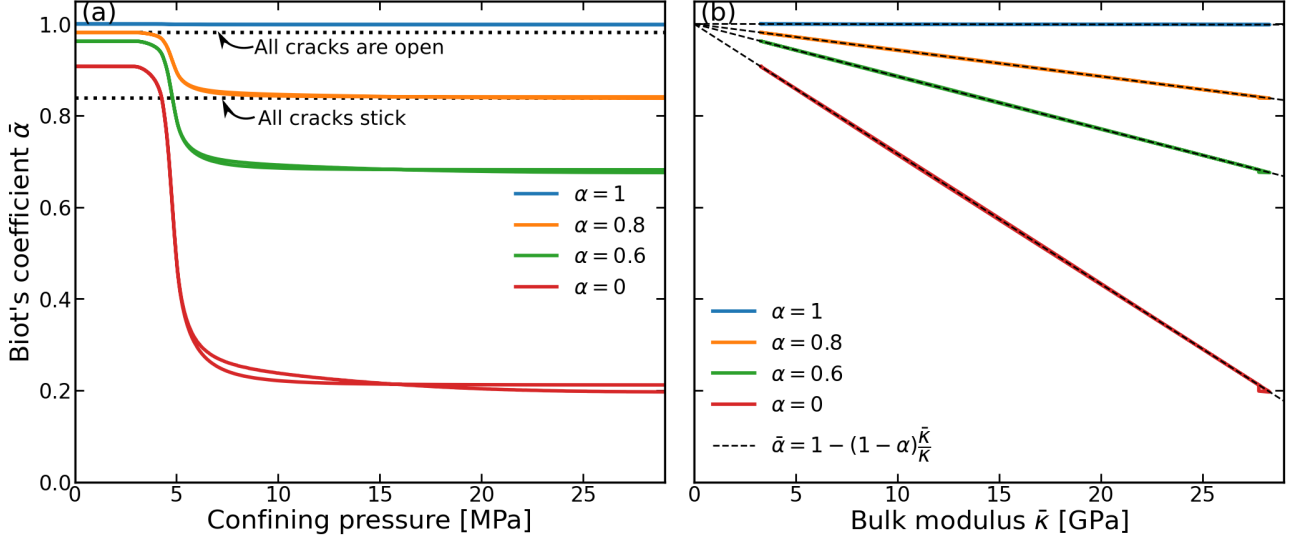
The evolution of Biot's coefficient is presented in Figure 6a to conclude the discussion on the effective properties of the assemblage. The data are exactly those considered for the reference curve in Figure 5 with a crack friction angle set to 30° and matrix Biot's coefficient equal to 0.8. The cyclic response is in line with the results presented in Figure 4, with a value close to 0.98 for low confining pressure as all cracks are open and around 0.84 for the largest values of the confining pressure resulting in the closure of most cracks. The exact asymptotic values are illustrated with the dotted lines. The blue and green curves are obtained for a larger and a smaller matrix Biot's coefficient compared to the reference value. The variation of this coefficient has no influence on the transition but controls the asymptotic value for large confining pressures. Note that there is a slight hysteresis during the cycle, which is more visible for the lowest value of the matrix Biot's coefficient. Moreover, the butterfly structure of this hysteresis is very analogous to the one observed for the bulk modulus in Figure 5 with a cross-over of the loading and unloading paths at approximately the confining pressure of 5 MPa. This analogy prompted the authors to plot Biot's coefficient as a function of the bulk modulus, Figure 5b. The variation is linear and given, up to numerical accuracy by:

$$\bar{\alpha} = 1 - (1 - \alpha) \frac{\bar{\kappa}}{\kappa}. \quad (28)$$

315 This linear response is, of course, a surprise, although it has been seen four times in this contribution while discussing
 316 analytical solutions. Consider first the case of all cracks closed and slipping in either forward or reverse mode, Equation
 317 (78) in Appendix G. The three other cases correspond to a homogeneous response within the shell with either all open
 318 cracks, all closed and sticking cracks or all closed and slipping with zero friction. For these homogeneous response,
 319 combine the shell effective Biot's coefficient in Equation (34) of Appendix A with Equation (26) and obtain indeed the
 320 result in (28). The surprise comes from the fact that (28) holds also for any crack activation pattern encountered during
 321 the cyclic loading. Proof of this statement¹, which is not given here, would require showing that the displacement field

¹A simple tentative argument could be proposed nevertheless, similar to the one followed to relate Biot's coefficient to the ratio

322 for complex crack response has the structure found in Equation (74). There are first a collection of terms function of the
 323 effective stress $\dot{\sigma}_H - \dot{p}_f$ and second, the last term found in this equation in all cases.
 324 The discussion above has highlighted the significant difference between the numerical predictions and the analytical
 325 solution for all cracks slipping in forward or reverse mode, especially for reasonable values of the friction parameter. This
 326 discrepancy to be resolved necessitates analyzing the cracks' response at a finer scale. The analysis is presented in the
 327 following section.



328 **Figure (6)** The cyclic evolution of the effective assemblage Biot's coefficient $\bar{\alpha}$ with the confining pressure for different
 329 values of matrix Biot's coefficient in a). The relation between the effective Biot's coefficient and bulk modulus is linear
 330 (equation 28) as shown with the dashed lines, b).

3.2 Crack's response around the cavity, drained conditions.

329 Figure 7 is proposed to analyze the response of the populations of cracks around the cavity. The two columns on the
 330 left illustrate the results for the two friction parameters of 0.01 and 0.6, respectively. The five rows of three graphs
 331 correspond to different values of the confining pressure, numbered from 1 to 5 (1 and 2 during loading and 3 to 5 during
 332 unloading) as defined in Figure 5a. Each graph in these two left columns presents the angle β_c , which marks the limit of
 333 open and closed cracks (dashed blue curve and values read on the right axis), as well as the proportion of cracks sliding
 334 in forward or reverse mode (red and black curve and values read on the right vertical axis). The column of graphs on
 335 the right of Figure 5a compares the crack's response for the two friction values (green and purple colors) at a specific
 336 distance of the pore center, which is set to 0.6281. The crack distribution (first polar angle β) ranges from zero to 90
 337 degrees, and the cracks are shown as either open, sticking, or slipping in forward or reverse mode.

338 The first point of comparison between the results for the two values of the friction coefficient is at the confining
 339 pressure of 6 MPa, the top row of Figures 7. The crack closure curve is similar for the two friction values. The crack
 340 orientations above the curves are closed and are open below. Cracks at radius larger than, approximately $0.77R_s$ are all
 341 closed. As the normalised radius is decreased below this 0.77, the population of open cracks increases. It is impossible
 342 to close all cracks since the normal stress for $\beta = 0$ is the radial stress, which is equal to the initial pore pressure at the
 343 pore wall. Among the closed cracks, the red curve indicates that for $\mu = 0.01$, 70% to 100 % of cracks slip as one moves
 344 away from the pore wall. For $\mu = 0.6$, less than 20% of cracks slip. Surprisingly, it is the cracks closest to the pore (i.e.,
 345 between $r = 0.5R_s$ and $0.6R_s$) that are activated. The left plot confirms this interpretation. At $r = 0.6281$, the same
 346 cracks are open, but the closed cracks slip for the low friction and stick for the large friction.

347 The second comparison is at the maximum loading for $\sigma_H = 30$ MPa and corresponds to the second row in Figures 7.
 348 All cracks are closed for a radius greater than $0.53R_s$, approximately. Only a few cracks near the pore remain open. If
 349 the friction is low, almost all the closed cracks slip. However, for the large friction only a small fraction of the cracks
 350 closest to the pore slip. The proportion is around 40% and decreases to zero for a radius close to $0.62R_s$. The plot to the
 351 right confirms the difference with all cracks sticking or slipping for the large and low friction, respectively, at $r = 0.6281$.

352 The three other comparisons are done during the unloading. During the initial stage (where σ_H equals 28.8 MPa and
 353 third row in Figure 7), the black curve indicates that the cracks experience an almost instantaneous reverse slip in the
 354 case of low friction. The proportion of reverse slipping cracks decreases with the radius. At the pore wall, approximately

of the effective bulk modulus to the skeleton bulk modulus. Consider Equation (24)a to describe the response of a comparison
 solid, meaning that it is valid for any fluid pressure rate and any remote pressure rate. Choose then $\dot{\sigma}_H = \dot{p}_f$ and conclude that
 $-(1 - \bar{\alpha})\dot{p}_f/\bar{\kappa} = \dot{\theta}$. This assemblage volumetric deformation rate can be estimated from a micro-scale point of view. The matrix
 sustains on its boundary a purely normal loading set to \dot{p}_f and thus develops a stress rate purely hydrostatic. Its volumetric rate
 is thus $(\alpha - 1)\dot{p}_f/\kappa$. The open cracks must sustain the same volumetric rate if still open. The deformation is thus the same,
 homogeneous, for the two phases, matrix and fluid phase, and thus equal to the assemblage $\dot{\theta}$. Combine these two results to obtain
 Equation 28.

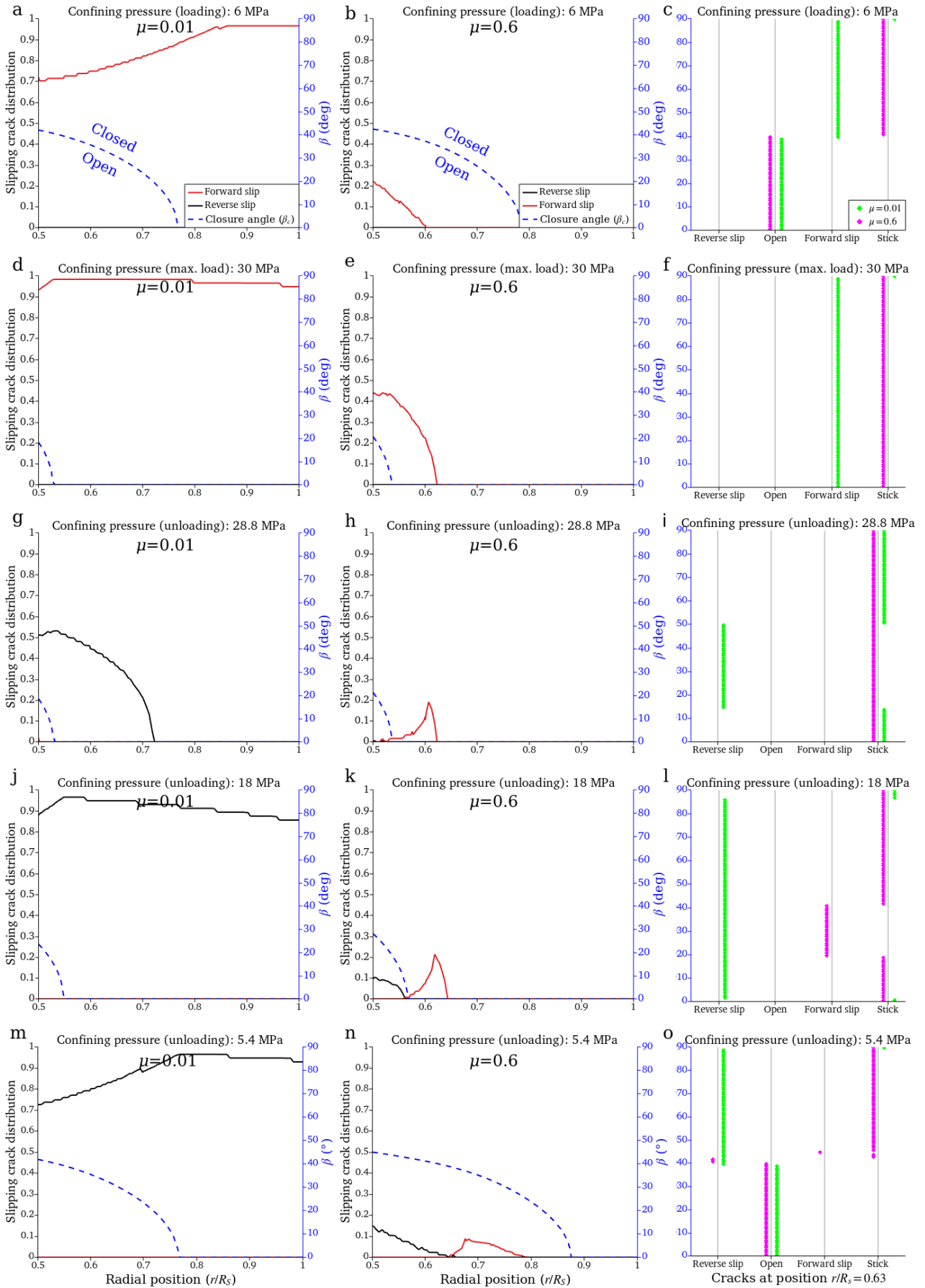


Figure (7) The crack slipping regime and distribution (proportion of slipping cracks) as a function of the radial position at five stages of the loading cycle defined in Figure 5. The left and central columns of plots for friction coefficient of 0.01 and 0.6, respectively. The dashed blue curve in each plot represents the crack closure angle β_c (right vertical axis). Above this angle, all cracks are closed, and below it, they are open. The red and black curves are the proportion of cracks slipping in forward of reverse mode (left vertical axis). The right column of plots shows the crack regime at a specific radius (r/R_s) in terms of the first polar angle β .

355 half of the cracks show reverse slipping. This proportion increases during further unloading and then decreases because
 356 of the reopening of the cracks as can be seen from Figure 7j and m. However, for the large friction (Figure 7h k and n)
 357 the response is very different with continuous forward slip of a population of cracks despite the overall unloading. Many
 358 cracks around $r = 0.6R_s$ continue to forward slip. This group of sliding cracks is getting translated towards the external
 359 part of the shell as unloading is pursued while the population for cracks with reverse slip is increasing from the pore.
 360 The other surprise is the observation at $r = 0.6281$, during the last phase of unloading, Figure 7o: there are at the same
 361 radius cracks slipping in either reverse or forward slip for an orientation close to 40 and 45 degrees, respectively.

362 3.3 Cyclic response with undrained conditions

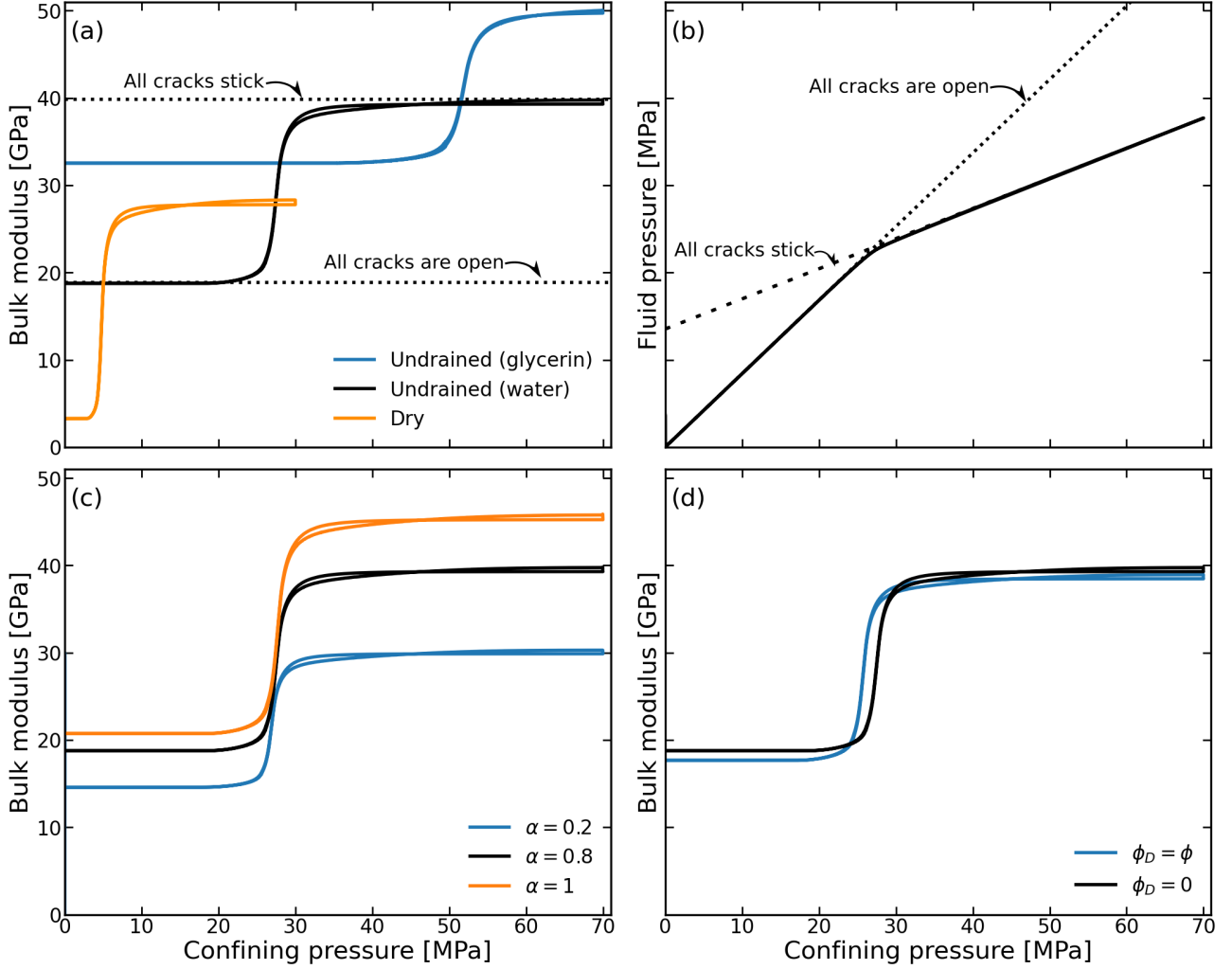


Figure (8) Bulk modulus for undrained conditions with water or glycerin and comparison with drained conditions in (a). Evolution of the pressure during a cycle with water in (b). Influence of the matrix Biot's coefficient in (c), and of the dead volume in (d).

363 The last set of results concerns the loading under undrained conditions. The first graph shown in Figure 8a compares
 364 the drained response to the undrained response for glycerin ($\kappa_f = 4.5$ GPa) and water ($\kappa_f = 2.2$ GPa). This comparison
 365 assumes a matrix Biot's coefficient of 0.8 and no dead volume. All other parameters are the same as those used in
 366 the reference simulation discussed earlier. The assemblage bulk modulus is significantly different from the drained case
 367 when all cracks are open or when most cracks are closed and sticking. The limiting cases of all open and all closed and
 368 sticking are represented by the dotted lines in the graph for the water-saturated case, and they are well matched by
 369 the numerical predictions. The other difference with the drained case is the transition between the two limits, which is
 370 delayed because of the fluid bulk modulus and the variation in fluid pressure. The delay becomes more significant as the
 371 fluid bulk modulus increases. Note also that increasing the fluid bulk modulus reduces the hysteresis effect. Although
 372 the micro-structure response is comparable to the one observed for drained conditions, the fraction of slipping cracks is
 373 less for undrained simulations.

374 The role of the variation in fluid pressure is presented in Figure 8b for the case of water. The variation is approximately
 375 bi-linear, starting from an initial value of 0.1 MPa and ending at approximately the value of the confining pressure. The
 376 analytical expressions for the Skempton coefficient found in Equation (20) work well for both all open and closed and
 377 sticking cracks, and they provide the slopes of the dotted and dashed lines starting either from the initial or the final
 378 pressure, as plotted in Figure 8b. It should be noted that although not visible on the graph, there is a slight hysteresis in

379 the fluid pressure variation. If the cracks are active, there is a maximum difference of 0.07 MPa in fluid pressure between
 380 loading and unloading.

381 Figure 8c and 8d present two additional plots that investigate the impact of the matrix Biot's coefficient and dead
 382 volume on the assemblage bulk modulus. The black reference curve corresponds to water and a matrix Biot's coefficient
 383 of 0.8. The two limiting values are influenced by the matrix Biot's coefficient. The larger the Biot's coefficient, the larger
 384 these limits are. However, this coefficient has no effect on the transition or the closing of the cracks. Figure 8d shows the
 385 impact of dead volume. Increasing ϕ_D results in a slight reduction in bulk modulus as well as a decrease in the confining
 386 pressure required to achieve the transition between the two limiting values.

387 There is a surprising result observed in Figure 8a which deserves further discussion. The bulk modulus at the end
 388 of the loading phase is close to 40 GPa and 50 GPa for the water and the glycerin. These two values are much larger
 389 than the matrix bulk modulus which is approximately 35 GPa. It is classically observed in rocks that the undrained
 390 bulk modulus does not exceed the dominant mineral bulk modulus. This difference is very sensitive to the matrix Biot's
 391 coefficient as can be seen from Figure 8c for the water: the critical value of α beyond which the assemblage modulus is
 392 greater than the matrix bulk modulus is between 0.2 and 0.8. If one assumes that all cracks are closed and sticking at
 393 the end of loading, then this critical value of α at which the two moduli are equal is found analytically and is 0.47 and
 394 0.78 for water and glycerin. This finding reveals some applicability limit of the proposed prototype to classical rocks.
 395 The matrix Biot's coefficient is set to zero in the next section and the results do not suffer from this limitation.

396 4 Application to hydrostatic compression of dry specimens

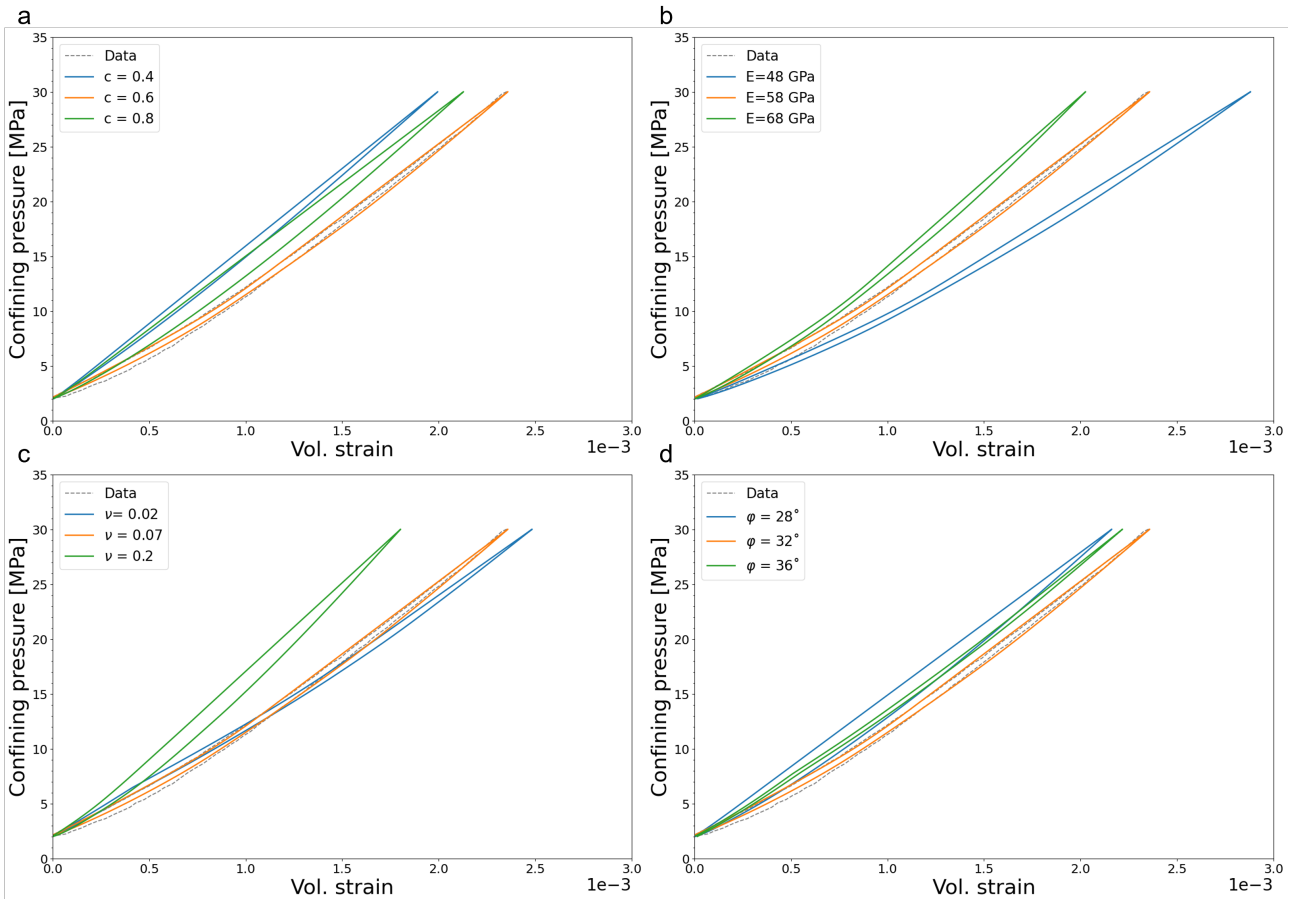


Figure (9) Volumetric strain versus confining pressure varying the crack density c , matrix elasticity modulus E , matrix Poisson's ratio ν , and friction angle φ in a to d. The best fit for Bentheim is obtained for $c = 0.6$, $\varphi = 32^\circ$, $\nu = 0.07$ and $E = 58$ GPa (orange curve). Note that the porosity is the same for all simulations and is equal to the real sample's porosity $\phi=22.2\%$, and that $\sigma_C = 2$ MPa.

397 The stress-strain curves from hydrostatic compression tests on dry samples are now simulated. The experimental
 398 data come from Chapman et al. [2023] and showcase four rock samples. The clean Bentheim sandstone (95% quartz) has
 399 a 22% porosity and a grain size between 18 and 500 μm . The Chauvigny limestone has a 16.2% porosity and is entirely
 400 composed of calcite. The two carbonates, C-2 and C-3, have a porosity of 17.1% and 14.7%, respectively. C-2 is granular
 401 and is mainly composed of calcite ($\geq 95\%$), whereas C-3 has a shub facies and contains a mix of calcite (45.5%), quartz
 402 (38.3%) and dolomite (15.2%).

403 In dry conditions, the numerical model takes six parameters as inputs: c , φ , ν , E , ϕ , and σ_C . The porosity is set to the
 404 one measured experimentally. The crack closure stress used in the model corresponds to the confining pressure at which

405 the hysteresis loop would close at the end of the loading cycle. It is inferred from the stress-strain curve. The matrix
 406 Poisson's ratio and internal friction compare to those of the principal mineral at room temperature. However, given that
 407 the value range of the elasticity modulus is quite large for common minerals (90-100 MPa for quartz and 90-150 MPa
 408 for calcite), E is used as a fitting parameter. Also, information about the crack density is not assessed experimentally
 409 and is thus a fitting parameter. A first analysis of the Bentheim sandstone is proposed below to understand the impact
 410 of all the parameters that are not strictly measured (E , c , φ , ν).

411 Figure 9 shows the influence of the matrix properties on the hysteresis loop for Bentheim at fixed $\sigma_C = 2$ MPa, and
 412 $\phi = 22.2\%$. In Figure 9a, (with $E = 58$ GPa, $\varphi = 32^\circ$, $\nu = 0.07$), increasing c from 0.4 to 0.8 leads to a smaller slope and
 413 a larger hysteresis. In Figure 9b (with $c = 0.6$, $\varphi = 32^\circ$, $\nu = 0.07$), the increase of E leads to the increase of the average
 414 slope and the decrease of the dissipated energy ΔE_n (loop area). Note that E has a greater impact on the slope than
 415 on ΔE_n . From Figure 9 (with $E = 58$ GPa, $c = 0.6$, $\varphi = 32^\circ$), observe that the increase in ν from 0.02 to 0.2 results in
 416 both a larger slope and ΔE_n . Figure 9d (with $E = 58$ GPa, $c = 0.6$, $\nu = 0.07$) shows that the increase in φ from 28° to
 417 36° results in the decrease in hysteresis, as well as the more concave curve. The best fit for the data, provided by the
 418 least square method with E and c as fitting parameters (at fixed $\varphi = 32^\circ$ and $\nu = 0.07$), is obtained at $E = 58$ GPa and
 419 $c = 0.6$ as shown by the orange curve. The predicted elasticity modulus is thus notably smaller than that of quartz.

420 The fitting considers the amount of hysteresis, which is a proxy for the energy dissipated by the sample, and is
 421 conventionally represented by the attenuation factor Q^{-1} . This attenuation factor is the ratio of the area of the hysteresis
 422 loop to the average energy stored in the sample (O'Connell and Budiansky [1978]). It stems from the direct definition
 423 of the attenuation factor as the ratio of the dissipated energy ΔE_n to the average energy V_n stored by the rock:

$$Q^{-1} = \frac{\Delta E_n}{4\pi V_n}, \quad (29)$$

424 a definition found in Borgomano et al. [2017] and that differs by a factor of two from similar definitions in classical
 425 contributions such as Knopoff [1964] and Jaeger et al. [2009]. In practical terms, ΔE_n is the area of the hysteresis
 426 loop, and V_n is the area below the loop; both areas were computed incrementally, following Tisato and Madonna [2012].
 427 The value retrieved from the reported data of Bentheim is $Q_{exp}^{-1} = 1.03 \times 10^{-2}$ and that of the numerical hysteresis is
 428 $Q_{num}^{-1} = 1.05 \times 10^{-2}$. This is a good match, considering the simplicity of the model and the difference is certainly below
 429 the experimental accuracy.

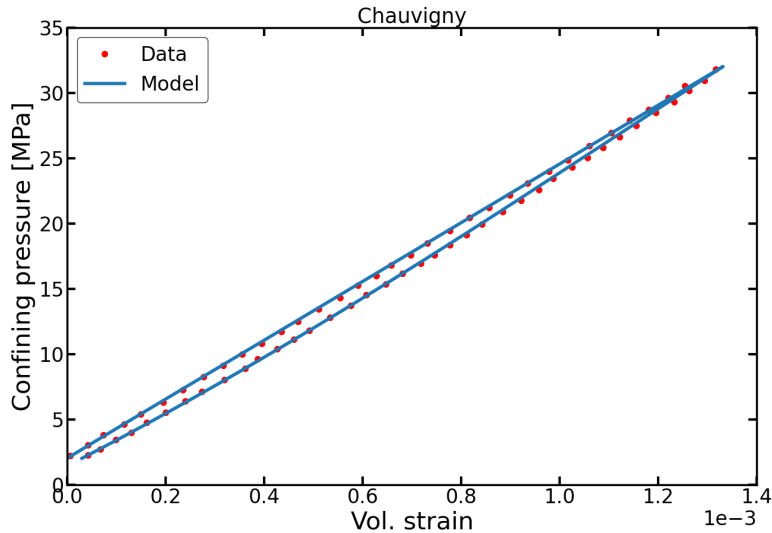


Figure (10) Volumetric strain versus confining pressure for Chauvigny. The fitting parameters are: $c = 0.4$, $\varphi = 32^\circ$, $\nu = 0.2$, $E = 61$ GPa, $\sigma_C = 2.5$ MPa and $\phi = 16.2\%$.

430 In addition to Bentheim, the numerical results for Chauvigny show a very good fit with $Q_{exp}^{-1} = 1.47 \times 10^{-2}$ and
 431 $Q_{num}^{-1} = 1.46 \times 10^{-2}$. Figure 10 displays the data and numerical volumetric strain versus confining pressure for Chauvigny.
 432 The numerical result corresponds to : $c = 0.4$, $\varphi = 32^\circ$, $\nu = 0.2$, $E = 61$ GPa, $\sigma_C = 2.5$ MPa, $\phi = 16.2\%$. Again, only c
 433 and E are fitting parameters since ϕ and σ_C are inferred from the data, and ν and φ are fixed for simplicity. Note that
 434 the experimental curve for Chauvigny is quite symmetrical and linear in loading versus unloading. This agrees with the
 435 frictional crack theory for a specimen with minor defects (small crack density) and spheroidal pores.

436 Regarding the other two carbonates, C-2 and C-3, the stress-strain curves are neither symmetrical nor quasi-linear.
 437 This makes using E and c as the only fitting parameters more difficult. Figure 11c and 11b show the best fit using
 438 two fitting parameters (E and c) for C-2 and C-3, respectively. Note that, although the amount of hysteresis is closely
 439 matched, the slopes are very different. Several factors can explain the curvier aspects of the C-2 and C-3 loops, notably
 440 the grain and pore shapes and the nature of the grain contacts. Unfortunately, no analysis of the pore shape is available
 441 for these samples. Nonetheless, the curvier aspect of the experimental loop suggests that the local deviatoric stress is
 442 quite large. Yet, the proposed prototype in this contribution uses a spherical pore to generate deviatoric stress which is
 443 thus controlled entirely by porosity. The measured porosities for C-2 and C-3 are too small to reproduce the data using
 444 this simple prototype. It is important to note that carbonates have complex micro-structures with varying grain shapes

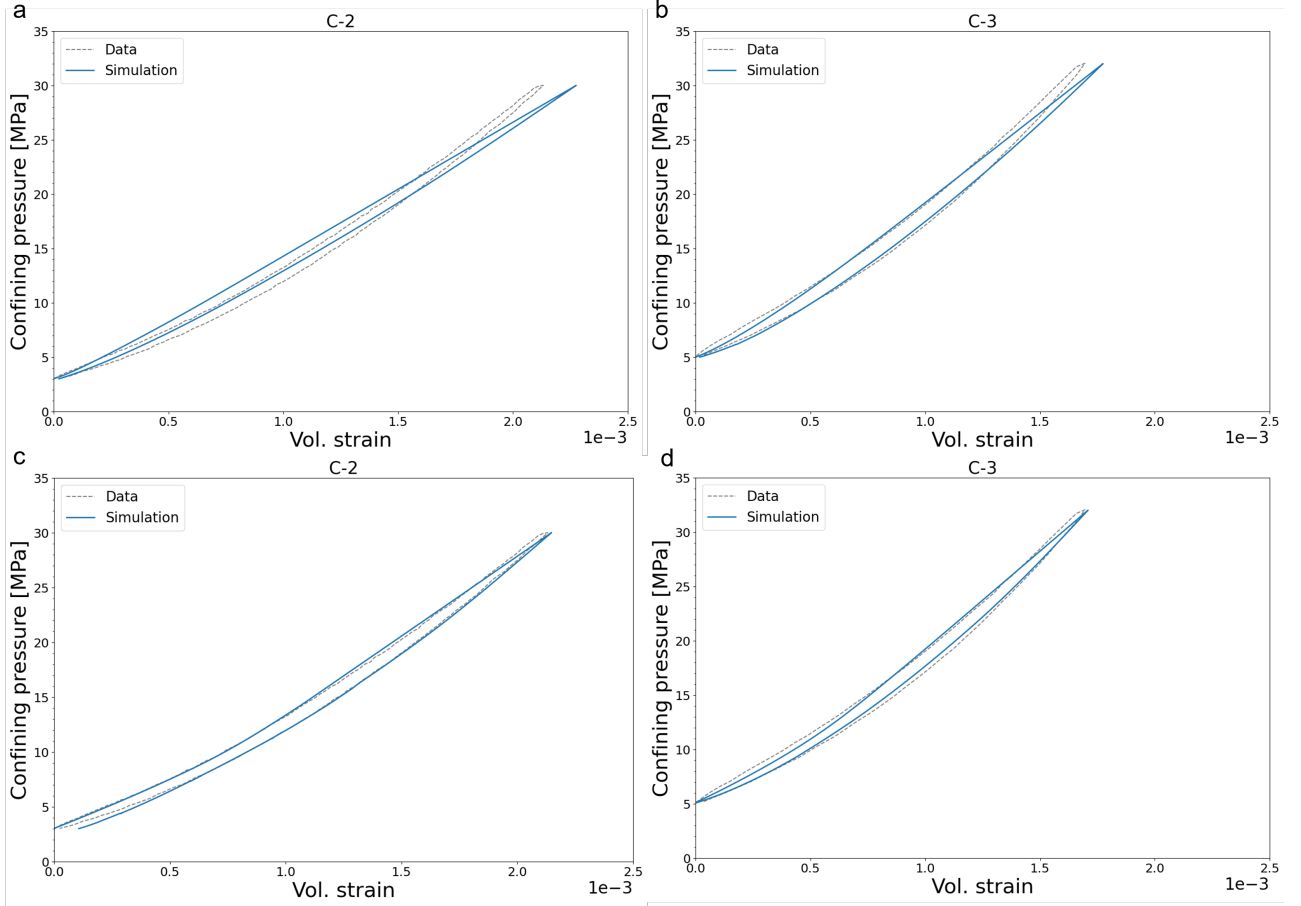


Figure (11) The experimental data of the hydrostatic compression cycle for C-2 and C-3 carbonates versus the theoretical curves. In a and b, the best fit when using only E and c as fitting parameters. In c and d, the best fit when using E , c , ϕ , μ and ν as fitting parameters.

Table (2) Best fitting parameters for the experimental data.

Parameter	Bentheim	Chauvigny	C-2	C-3
E [GPa]	57	61	80	68
ν	0.07	0.20	0.20	0.20
φ [°]	32	32	41	30
c	0.60	0.40	0.8	0.5
σ_C [MPa]	2	1	3	5
ϕ [%]	22.2	16.2	43.0	28

445 and micro-porosities of different types not accounted for. Additionally, when closely examining the curves for C-2 and
446 C-3 (Figure 3e and 3f of Chapman et al. [2023]) at higher confining pressures, it is evident that there is an evolving
447 strain at a constant pressure of 30 MPa, which resembles creep-like behaviours. These behaviours are not observed in
448 the other rocks and could be due to minerals' plasticity, which is not accounted for. To address this limitation, one can
449 either increase the porosity in the model or flatten the central pore. The former solution was adopted to fit the data
450 since further development would be needed to try the latter. Figure 11c and 11d show the best fits for C-2 and C-3 by
451 optimising E , c , ϕ , μ and ν . These best-fitting parameters are provided in Table 2.

5 Conclusion

A model problem to capture the hysteresis in hydrostatic compression tests has been proposed. It is built with two homogenization schemes, the first at the REV scale within the shell material and the second for the assemblage composed of the pore, the shell and the homogeneous effective medium. It considers uniform pore-fluid pressure at the assemblage length scale for either drained or undrained conditions, the fluid mass within the specimen and the additional dead volume being constant in the latter case.

The hysteresis is analysed by plotting the bulk modulus during the loading cycle versus the remote compressive stress. Four stages labeled (i) to (iv) are observed during a typical cycle. Stage (i) applies during the early phase of compression as well as during the late stage of unloading since all cracks are open. Stage (ii) corresponds to the end of loading when the population of closed, slipping cracks is then stabilized. Stage (iii) signals the beginning of unloading and most of the closed cracks are sticking. Stage (iv) marks a stage closer to the initial conditions with the reopening of cracks and slipping of the closed cracks. Four analytical solutions are proposed for open cracks (stage i), all cracks closed and sticking and also for all cracks closed and slipping in either forward or reverse mode. The two latter solutions were expected to capture stages (ii) and (iv). The finite-element solution enables to capture the transitions between these various stages and to assess the validity of the assumptions behind the analytical solutions.

The finite-element solution in stage (i) and (iii) matches the analytical solution. The asymptotic values are functions of the matrix elasticity and the crack properties for the drained case and in addition, of the fluid bulk modulus and matrix Biot's coefficient for undrained conditions. Surprisingly, the new analytical solution for all slipping cracks is only reasonably matched for low friction angle. Two of the assumptions considered for the analytical development are seen not to be valid. First, in all cases, there is always a small shell around the pore where cracks do not close because they are oriented such that their normal stress is close to the radial stress and thus controlled by the pore pressure. The second reason is that all cracks do not stick at the reversal of the assemblage confining pressure. There is indeed a zone where forward slip is pursued during the early phase of unloading. This zone extent is shifted towards the assembly outer radius as reverse slip is initiated closer to the pore during the unloading. Moreover, it is observed that at critical radii, the population of cracks could be in the four states: open, closed and sticking, closed and slipping forwardly or reversely, depending on their orientation.

The finite-element solution for the assemblage Biot's coefficient is proposed for drained conditions and thus constant fluid pressure. It is based on the ratio of the fluid volume rate of change (pore volume fraction rate) to the assemblage volume. This Biot's coefficient is found to be an affine function of the assemblage bulk modulus. This same relation was indeed derived for the the four analytical solutions but not shown to prevail for general crack states.

The finite-element predictions also reveal the key parameters controlling the transition between stage (i) and stages (ii) and (iii), which marks the crack closure. The main parameter is the crack closure stress although the crack concentration has also a minor influence. For undrained conditions, the fluid bulk modulus becomes a key parameter, while the matrix Biot's coefficient as well as the dead volume, have a minor influence.

The fitting of experimental data from the hydrostatic compression of dry sandstones and carbonates presented by [Chapman et al. \[2023\]](#) is done in two optimisations using the least square method on the stress-strain data. The first optimisation uses only the matrix elasticity modulus and the crack density, while the second optimization makes use of all six parameters (assemblage porosity, crack stress closure, crack friction, Biot's coefficient, the elasticity modulus and Poisson's ratio of the matrix). Using the first optimization, we could predict the hysteresis loops of the Bentheim sandstone and Chauvigny limestone. We observed that the quality of the fit of the transitional phase between (i) and (ii) is a function of the deviatoric stress generated by the central pore. A bigger central pore leads to a longer transition. However, the specimen's porosity in the central pore did not cause enough deviatoric stress to match the data from the C-2 and C-3 carbonates. For these two samples, the second optimization (including a considerable increase in the porosity), results in a good fit. The model seems to perfectly predict the hysteresis loop of porous samples ($\phi \geq 10\%$).

The application of this model problem could be extended in different directions and two are now briefly discussed. The first direction is due to the inability of this micro-structural model to match the experimental results for low porosity rock, as observed for the Granite and for two of the carbonates tested by [Chapman et al. \[2023\]](#). One could wonder if visco-plasticity could explain the issue for the latter and it is clear that the spherical pore should be replaced by another source of deviatoric stress such as, for example, the interaction of an isotropic distribution of frictional cracks, for the former. Second, this micro-structural model is now validated for porous rocks and should be applied to capture the strain amplitude dependence of the static elastic properties [[Pimienta et al., 2015](#)]. This effort will require a change in the numerical scheme to accommodate an oedometric loading condition thus switching from radial to cylindrical symmetry. This generalization is also required for hydrostatic loading if a comparison between static and dynamic properties (V_P and V_S) is intended. The determination of the dynamic shear response of the assemblage needs the shear effective property which could indeed be deduced assuming a cylindrical symmetry and a P-wavelength long compared to the assemblage length scale.

508 **CRedit authorship contribution statement**

509 **Alvin T. Biyoghé:** Conceptualization, Methodology, Software, Validation, Investigation, Data fitting, Writing – original
510 draft,

511 **Yves M. Leroy:** Conceptualization, Methodology, Software, Writing – review & editing, Supervision.

512 **Lucas Pimienta:** Conceptualization, Methodology, Validation, Data fitting, Writing – review,

513 **Robert W. Zimmerman:** Conceptualization, Methodology, Writing – review & editing, Supervision.

514 **Declaration of competing interest** The authors declare that they have no known competing financial interests or
515 personal relationships that could have appeared to influence the work reported in this paper.

516 **Data availability** The data used for the research described in the article has been referenced appropriately.

517 **Acknowledgment** All authors have seen and approved the final version of the manuscript being submitted. Work at
518 Imperial College London of Yves M. Leroy was supported by TotalEnergies S.E. Helpful discussions with Jan Borgomano
519 (TotalEnergies S.E., CSTJF, Pau) and Jérôme Fortin (Laboratoire de Géologie, ENS, Paris) are gratefully acknowledged.
520 Lucas Pimienta was supported by the chair E2S-ANR (Thermapp).

Appendices

A Elasticity solution

The elasticity solution is fundamental to this contribution, and the porous, homogeneous material composing the shell is linearly elastic, isotropic with equivalent properties $(\kappa^*, G^*, \alpha^*)$. The initial state corresponds to a pressure set to p_{f0} , isotropic stress equal to $-p_{f0}$, and is associated with zero deformation and displacement.

The solution is found with the displacement method. The displacement is radial, and thus of the type $\underline{u}(r) = u(r)\underline{e}_r$ with the scalar function $u(r)$ of the radial position with respect to the center of the pore as the only unknown. The only non-zero linearized strain components are:

$$\epsilon_r = u_{,r}, \quad \epsilon_\theta = \epsilon_\varphi = \frac{u}{r}, \quad (30)$$

with a comma standing for the partial derivative for the variable that follows. The volumetric strain is the sum of these three components: $\epsilon_v = u_{,r} + 2\frac{u}{r}$. The poro-elasticity constitutive relations for an isotropic medium are now applied, and the stress field in terms of the displacement function or its gradient and the fluid pressure reads:

$$\begin{aligned} \sigma_r + p_{f0} &= (\kappa^* - \frac{2G^*}{3})\epsilon_v + 2G^*u_{,r} - \alpha^*(p_f - p_{f0}), \\ \sigma_\theta + p_{f0} = \sigma_\varphi + p_{f0} &= (\kappa^* - \frac{2G^*}{3})\epsilon_v + 2G^*\frac{u}{r} - \alpha^*(p_f - p_{f0}). \end{aligned} \quad (31)$$

This stress field satisfies point-wise mechanical equilibrium, which, because of the problem symmetry, is expressed by a single equation:

$$\sigma_{r,r} + \frac{1}{r}(2\sigma_r - \sigma_\theta - \sigma_\varphi) = 0. \quad (32)$$

Insert now the expressions in (31) in this equilibrium equation to obtain a second-order differential equation for the unknown function $u(r)$. The solution is found by integration and reads:

$$u(r) = Ar + \frac{B}{r^2}, \quad (33)$$

for two constants A and B . The stress components in terms of these constants read:

$$\sigma_r + p_{f0} = 3\kappa^*A - 4G^*\frac{B}{r^3} - \alpha^*(p_f - p_{f0}), \quad \sigma_\theta + p_{f0} = \sigma_\varphi + p_{f0} = 3\kappa^*A + 2G^*\frac{B}{r^3} - \alpha^*(p_f - p_{f0}). \quad (34)$$

The constants are found by imposing that the remote stress is the hydrostatic pressure σ_H (positive scalar in compression) while the radial stress at the pore surface is minus the fluid pressure p_f :

$$A3\kappa^* = -(p_f - p_{f0})(1 - \alpha^*) - \frac{(\sigma_H - p_f)}{1 - \phi}, \quad B = -\frac{(\sigma_H - p_f)}{4G^*} \frac{R_P^3}{1 - \phi}. \quad (35)$$

The stress fields finally read:

$$\sigma_r = -p_f - \frac{(\sigma_H - p_f)}{1 - \phi} \left(1 - \left(\frac{R_P}{r}\right)^3\right), \quad \sigma_\theta = \sigma_\varphi = -p_f - \frac{(\sigma_H - p_f)}{1 - \phi} \left(1 + \frac{1}{2}\left(\frac{R_P}{r}\right)^3\right). \quad (36)$$

The effective properties of the spherical assemblage defined in (24) are in terms of the assemblage volumetric strain, θ , which is equal to $3u_r(R_S)/R_S$ for small perturbations. This volume change for the assemblage is found by combining (33) and (35):

$$\theta = -(1 - \alpha^*)\frac{p_f - p_{f0}}{\kappa^*} - \frac{(\sigma_H - p_f)}{1 - \phi} \frac{4G^* + 3\kappa^*\phi}{4G^*\kappa^*}. \quad (37)$$

This relation between volume change and pressure and remote stress σ_H provides the effective medium properties as defined in equation (24) and presented in (26).

B Effective properties of an elastic medium with an isotropic distribution of open, circular cracks

The stress-strain relation (1) with the introduction of the crack compliance tensor in (2) reads:

$$\begin{aligned} \underline{\dot{\epsilon}} &= \mathbb{C} : (\underline{\dot{\epsilon}} + \alpha \dot{p}_f \underline{\delta}) + \frac{c\gamma\pi}{2l} \left\{ \underline{\underline{N}} \cdot (\underline{\dot{\epsilon}} + \dot{p}_f \underline{\delta}) + (\underline{\dot{\epsilon}} + \dot{p}_f \underline{\delta}) \cdot \underline{\underline{N}} - \nu \mathbb{N} : (\underline{\dot{\epsilon}} + \dot{p}_f \underline{\delta}) \right\}, \\ \text{with } \underline{\underline{N}} &= \int_{\mathcal{H}} \underline{n} \otimes \underline{n} d\mathcal{H} \quad \text{and} \quad \mathbb{N} = \int_{\mathcal{H}} \underline{n} \otimes \underline{n} \otimes \underline{n} \otimes \underline{n} d\mathcal{H}, \end{aligned} \quad (38)$$

the normal \underline{n} being defined by:

$$\underline{n} = \cos \beta \underline{e}_r + \sin \beta (\sin \beta' \underline{e}_\varphi + \cos \beta' \underline{e}_\theta), \quad (39)$$

in terms of the polar angles (β, β') . In equation (38), Biot effective stress is introduced for the matrix response, while the Terzaghi effective stress is proposed for the crack response. The second-order \underline{N} is isotropic so proportional to the identity tensor $\underline{\delta}$ with a proportionality factor of $2\pi/3$ found as follows:

$$\underline{N} \cdot \underline{e}_r = \int_{\mathcal{H}} \underline{n} \cos \beta d\mathcal{H} = \int_{\beta=0}^{\pi/2} \int_{\beta'=0}^{2\pi} \left[\cos^2 \beta \underline{e}_r + \sin \beta \cos \beta (\cos \beta' \underline{e}_\theta + \sin \beta' \underline{e}_\varphi) \right] \sin \beta d\beta' d\beta = \frac{2\pi}{3} \underline{e}_r. \quad (40)$$

The fourth-order tensor \mathbb{N} is also isotropic and has thus the following spectral decomposition:

$$\mathbb{N} = 3k\mathbb{J} + 2g\mathbb{K}, \quad (41)$$

in which k and g are two unknowns and the orthogonal tensors \mathbb{J} and \mathbb{K} defined by $\mathbb{J} = 1/3\delta \otimes \delta$ and $\mathbb{K} = \mathbb{I}_s - \mathbb{J}$ with \mathbb{I}_s standing for the symmetric, fourth-order identity tensor. The first constant k introduced in (41) is found by using the orthogonality property $\mathbb{N} : \mathbb{J} = 3k\mathbb{J}$ which, using the definition in (38b):

$$\mathbb{N} : \mathbb{J} = \frac{1}{3} \int_{\mathcal{H}} \underline{n} \otimes \underline{n} \underline{n} \cdot \underline{n} d\mathcal{H} \otimes \underline{\delta} = \frac{2\pi}{9} \underline{\delta} \otimes \underline{\delta} = \frac{2\pi}{3} \mathbb{J} \Rightarrow 3k = \frac{2\pi}{3}. \quad (42)$$

The second constant is found by considering another symmetry property of \mathbb{N} which is that all indices of its components in a Cartesian coordinate system can be permuted. The components of the isotropic tensor \mathbb{N} must have equal weight, such as in the expression

$$\delta_{ij}\delta_{kl} + \delta_{ik}\delta_{jl} + \delta_{il}\delta_{jk}, \quad (43)$$

which are the components of the tensor:

$$5\mathbb{J} + 2\mathbb{K}. \quad (44)$$

537 The ratio 5/2 between the scalars multiplying the two orthogonal tensors above is respected in (41) if $g = 3k/5$ providing
538 the value of the second unknown scalar $2g = 4\pi/15$.

539 The expressions for the tensor \underline{N} and \mathbb{N} are now inserted back in equation (38) to obtain the effective moduli κ^* and
540 G^* and the effective Biot's coefficient α^* :

$$\begin{aligned} \underline{\dot{\epsilon}} &= \left[\frac{1}{3\kappa^*} \mathbb{J} + \frac{1}{2G^*} \mathbb{K} \right] : (\underline{\dot{\sigma}} + \alpha^* \dot{p}_f \underline{\delta}) \\ \text{with } \frac{1}{3\kappa^*} &= \frac{1}{3\kappa} + \frac{c\pi^2\gamma}{3l}(2-\nu), \quad \frac{1}{2G^*} = \frac{1}{2G} + \frac{2c\pi^2\gamma}{3l}\left(1-\frac{\nu}{5}\right), \\ &\text{and } \alpha^* = 1 - (1-\alpha)\frac{\kappa^*}{\kappa}. \end{aligned} \quad (45)$$

541 C Finite-element solution

542 The starting point of the finite-element method is the theorem of virtual work, which equates internal and external
543 virtual works and reads in 3D:

$$\int_{\Omega} \underline{\underline{\sigma}}_{n+1} : \underline{\underline{\tilde{\epsilon}}} dV = \int_{\partial\Omega^T} \underline{T}_{n+1}^d \cdot \underline{\underline{u}} dS \quad (46)$$

544 in which Ω and $\partial\Omega^T$ are the assemblage domain and the part of its boundary where forces are prescribed. A superposed
545 tilde in equation (46) denotes the virtual strain and displacement. Time has been discretized, and the theorem is written
546 at the end of the increment $n+1$. The three objectives are to reduce this equation to the 1D setting appropriate for our
547 spherically symmetric problem, introduce the finite-element discretization, and discuss the time discretization.

548 The domain is limited to the extent of the matrix since the fluid is always in equilibrium within the pore. It is
549 also discretized in the radial direction with a series of finite elements. Spectral elements have been selected because of
550 the interesting property that nodal points and the Lobatto quadrature points coincide. The shape functions $N_a(r)$ at
551 node a have the properties that $N_a(r_b) = \delta_{ab}$ for any node positioned at r_b . The radial displacement over any element
552 is interpolated by the sum $u(r) = \sum_a^N N_a(r)$ over the total number of nodes per element N . The strain components
553 computed within each element are the radial and twice the hoop strain. They composed the column vector $\{\epsilon\}$. This
554 vector is obtained by the operation:

$$\{\epsilon\} = [B]\{u\}, \quad \text{with } [B] = \left[\dots \left| \begin{array}{c} N_{a,r}(r_b) \\ \frac{2}{r_b} \delta_{ab} \end{array} \right| \dots \right], \quad (47)$$

555 in which $[B]$ is the classical B-operator (defined at node b for a varying between 1 and the number of nodes in each
556 element) and the column vector $\{u\}$ contains the N nodal radial displacement of the element.

The stress at time t_{n+1} introduced in equation (46) is found from the update algorithm discussed in Appendix D for open cracks and in Appendix E for the sliding cracks. These updates correspond to a generic relation of the type:

$$\{\sigma\}_{n+1} = \{\sigma\}_n + [\mathbb{C}^{ec}]^{-1} \{\Delta\epsilon\} - \alpha \Delta p_f \{1\}, \quad (48)$$

557 in which the stress vector increment $\{\Delta\sigma\}$ and the unit vector $\{1\}$ have for components $\Delta\sigma_r, \Delta\sigma_\theta$ and 1, 1, respectively.
558 This equation is non-linear since the crack compliances, corresponding to the matrix $[\mathfrak{C}^{ec}]$, are a function of the stresses
559 at the end of the time step and are thus solved iteratively. This equation is now inserted in the theorem of virtual work
560 in (46), and the contribution of a single element Ω^e to the global system of equations resulting from the finite-element
561 discretization reads:

$$\int_{\Omega_e} {}^t[B]\{\sigma\}_{n+1} r^2 dr = T_{n+1}^d r^2|_{\partial\Omega_e^T}. \quad (49)$$

Note that the applied force T_{n+1}^d on the element boundary $\partial\Omega_e^T$ is the remote stress $-\sigma_{H_{n+1}}$ on the external radius R_S (last node of the last element for a mesh constructed from the internal to the external radii) and the pore pressure $+p_{f_{n+1}}$ at the pore wall (first node of the first element). Note also that equation (49) is non-linear and is solved by a Newton-Raphson search to satisfy equilibrium at the end of the time step t_{n+1} . The stress at iteration $(k+1)$ of the $n+1$ iteration, $\{\sigma\}_{n+1}^{(k+1)}$ is the sum of the stress at previous iteration $\{\sigma\}_{n+1}^{(k)}$ plus a perturbation $\{\delta\sigma\}$. This stress perturbation is related to the perturbation in strain $\{\delta\epsilon\}$ by a linearization of the constitutive relations in (48):

$$\{\delta\sigma\} = [\mathfrak{C}^{ec}]^{-1}\{\delta\epsilon\}. \quad (50)$$

562 The perturbation in strain is related to the displacement perturbation $\{\delta u\}$ by the B-operator introduced in (47) so that
563 the linearized set of equations to solve at each iteration is:

$$\int_{\Omega_e} {}^t[B][\mathfrak{C}^{ec}]^{-1}[B] r^2 dr \{\delta u\} = T_{n+1}^d r^2|_{\partial\Omega_e^T} - \int_{\Omega_e} {}^t[B]\{\sigma\}_{n+1}^{(k)} r^2 dr. \quad (51)$$

564 Note that the stiffness used in (51) and introduced in (50) should result from a consistent linearization of (48). It is
565 preferred here to keep with the inverse of the compliance set up at the end of the iterative update at the risk of not
566 getting a quadratic convergence rate. The number of iterations remains small (2 to 3) with a convergence tolerance of
567 10^{-7} .

568 D Numerical algorithm for cracks aperture update

569 This Appendix concerns the numerical algorithm to capture the evolution of the apertures of the isotropic distribution of
570 cracks. The starting point is again the stress-strain relation in (1) with the introduction of the crack compliance tensor
571 in (2):

$$\begin{aligned} \underline{\dot{\epsilon}} &= \mathfrak{C} : (\underline{\dot{\epsilon}} + \alpha \dot{p}_f \underline{\delta}) + \frac{c\gamma\pi}{2l} \left\{ \underline{N}_O \cdot (\underline{\dot{\epsilon}} + \dot{p}_f \underline{\delta}) + (\underline{\dot{\epsilon}} + \dot{p}_f \underline{\delta}) \cdot \underline{N}_O - \nu \mathbf{N}_O : (\underline{\dot{\epsilon}} + \dot{p}_f \underline{\delta}) \right\}, \\ \text{with } \underline{N}_O &= \int_{\mathcal{H}_O} \underline{n} \otimes \underline{n} d\mathcal{H} \quad \text{and} \quad \mathbf{N}_O = \int_{\mathcal{H}_O} \underline{n} \otimes \underline{n} \otimes \underline{n} \otimes \underline{n} d\mathcal{H}, \end{aligned} \quad (52)$$

572 The integration range is now limited to the part of the hemisphere \mathcal{H}_O corresponding to open cracks. The first cracks
573 to close as the remote loading increases are those aligned with the radial direction. The last ones to close are those
574 perpendicular to the radial direction. Consequently, the integration in terms of the two polar angles defined in Figure 3
575 corresponds to the range $\{\beta, \beta'\} = [0; \beta_c] \times [0; 2\pi]$ with β_c corresponding to the condition of crack closure in (4):

$$\cos^2 \beta_c (\sigma_r + p_f) + \sin^2 \beta_c (\sigma_\theta + p_f) = -\sigma_C \quad \text{with } \beta_c \in [0; \frac{\pi}{2}]. \quad (53)$$

576 The quadrature in β' is always from 0 to 2π because of the problem spherical symmetry. The result of the computation
577 of these two quadratures proposed in a matrix notation reads:

$$\begin{aligned} \begin{Bmatrix} \dot{\epsilon}_r \\ 2\dot{\epsilon}_\theta \end{Bmatrix} &= \frac{1}{9G\kappa} \begin{bmatrix} G + 3\kappa & 2G - 3\kappa \\ 2G - 3\kappa & 4G + 3\kappa \end{bmatrix} \begin{Bmatrix} \dot{\sigma}_r + \alpha \dot{p}_f \\ \dot{\sigma}_\theta + \alpha \dot{p}_f \end{Bmatrix} + \frac{c\gamma\pi^2}{l} \times \\ &\begin{bmatrix} \frac{2}{3}(1 - \cos^3 \beta_c) - \frac{\nu}{5}(1 - \cos^5 \beta_c) & -\frac{\nu}{5}[\frac{2}{3} - \frac{5}{3} \cos^3 \beta_c + \cos^5 \beta_c] \\ -\frac{\nu}{5}[\frac{2}{3} - \frac{5}{3} \cos^3 \beta_c + \cos^5 \beta_c] & \frac{\nu}{5}[\cos^5 \beta_c - \frac{10}{3} \cos^3 \beta_c + 5 \cos \beta_c - \frac{8}{3}] \end{bmatrix} \begin{Bmatrix} \dot{\sigma}_r + \dot{p}_f \\ \dot{\sigma}_\theta + \dot{p}_f \end{Bmatrix}. \end{aligned} \quad (54)$$

578 Two ways to check the components of the second matrix in (54): if all cracks are closed ($\beta_c = 0$), the components are all
579 equal to zero and less trivial; if all cracks are open ($\beta_c = \pi/2$) the system in (54) is then consistent with the findings in
580 Appendix B.

Time is now discretized, and equation (54) is written at the end of increment $n+1$ at which the strain vector and the fluid pressure are proposed during an incremental Newton-Raphson search for mechanical equilibrium:

$$\begin{Bmatrix} \Delta\epsilon_r \\ 2\Delta\epsilon_\theta \end{Bmatrix} + \frac{1-\alpha}{3\kappa} \Delta p_f \begin{Bmatrix} 1 \\ 2 \end{Bmatrix} = \begin{bmatrix} \mathfrak{C}^{ec}(\beta_c(t_{n+1})) \end{bmatrix} \begin{Bmatrix} \Delta\sigma_r + \Delta p_f \\ \Delta\sigma_\theta + \Delta p_f \end{Bmatrix}, \quad (55)$$

581 in which the components of the matrix \mathfrak{C}^{ec} are the sums of the components of the two matrices found in (54). The
582 difficulty for solving (55) to obtain the stress state at time t_{n+1} is that these components are functions of the angle β_c
583 defined in (53), which, in turn, is a function of the stress. It is proposed to solve this implicit system with a fixed-point
584 iterative process. A tolerance on the stress norm variation is set to 10^{-7} to define convergence.

E Numerical algorithm for frictional cracks update

The objective is to complement the algorithm presented in Appendix D to account for the displacement by slip over the closed cracks.

The resolved shear stress defined in equation (6) is related to the specific stress state of this problem:

$$\underline{\tau} = (\sigma_r - \sigma_\theta) \sin \beta \cos \beta \underline{p} \quad \text{with} \quad \underline{p} = \sin \beta \underline{e}_r - \cos \beta (\cos \beta' \underline{e}_\theta + \sin \beta' \underline{e}_\varphi), \quad (56)$$

in terms of the unit vector \underline{p} , perpendicular to the normal direction \underline{n} , and defined by the two polar angles β and β' introduced in Figure 2. The displacement jump across a given crack defined in (7) is proportional to the backstress rate $\dot{\underline{\omega}}$. This vector is now defined in terms of its component and the unit vector \underline{p} : $\dot{\underline{\omega}} = \dot{\omega} \underline{p}$ where $\dot{\omega}$ is a function of the first polar angle β and not of the second β' because of the problem symmetry. This rate $\dot{\underline{\omega}}$ should also be oriented along the unit vector \underline{m} defined in (8) by the normalisation of the vector $\underline{\tau} - \underline{\omega} = ((\sigma_r - \sigma_\theta) \sin \beta \cos \beta - \omega) \underline{p}$. We thus have $s = \underline{m} \cdot \underline{p}$ which is the sign of the scalar $(\sigma_r - \sigma_\theta) \sin \beta \cos \beta - \omega$. The direction of the vector $\dot{\underline{\omega}}$ being now defined the positive rate $\dot{\lambda} = s \dot{\omega}$ is obtained from the consistency of the condition (9) during continuous slip:

$$\dot{\lambda} = s(\dot{\sigma}_r - \dot{\sigma}_\theta) \sin \beta \cos \beta + \mu(\dot{\sigma}_r \cos^2 \beta + \dot{\sigma}_\theta \sin^2 \beta + \dot{p}_f). \quad (57)$$

The strain rate due to the slipping cracks according to (1) with (57) is then:

$$\frac{c\gamma\pi}{2l} \int_{\mathcal{H}_S} (\underline{n} \otimes \underline{p} + \underline{p} \otimes \underline{n}) ((\dot{\sigma}_r - \dot{\sigma}_\theta) \sin \beta \cos \beta + s\mu(\dot{\sigma}_r \cos^2 \beta + \dot{\sigma}_\theta \sin^2 \beta + \dot{p}_f)) \chi(\dot{\lambda}) d\mathcal{H}, \quad (58)$$

in which the quadrature is over \mathcal{H}_S , the part of the hemisphere \mathcal{H}_C where cracks are closed and the slip condition is respected (χ is the Heaviside function). In other words, equation (58) applies to the closed cracks and only if the scalar in (57) is positive. Note that this scalar is independent of the second polar angle β' and that the quadrature in (58) can be reduced to the first polar angle. The strain rate vector due to slip then reads:

$$\begin{Bmatrix} \dot{\epsilon}_r^s \\ 2\dot{\epsilon}_\theta^s \end{Bmatrix} = \frac{2c\gamma\pi^2}{l} \int_{\beta_c}^{\pi/2} \chi(\dot{\lambda}) \begin{bmatrix} \cos \beta (\sin \beta + \mu s \cos \beta) & -\sin \beta (\cos \beta - \mu s \sin \beta) \\ -\cos \beta (\sin \beta + \mu s \cos \beta) & +\sin \beta (\cos \beta - \mu s \sin \beta) \end{bmatrix} \sin^2 \beta \cos \beta d\beta \begin{Bmatrix} \dot{\sigma}_r + \dot{p}_f \\ \dot{\sigma}_\theta + \dot{p}_f \end{Bmatrix}, \quad (59)$$

using a matrix notation. Further analytical developments are challenging for an arbitrary loading because backstress varies with β and is not defined by macro-scale variables. It is thus preferred, for the sake of simplicity, to propose the following numerical quadrature of (59): divide the range of β which is $[0; \pi/2]$ in k intervals. For each i^{th} interval, consider the orientation $\beta = (i - 1/2)\pi/(2k)$ and if the closing condition is respected and the slip criterion exceeded, check the sign of $\dot{\lambda}$ in (57). If the sign is positive, add the contribution of the left-hand side of (59) to the matrix \mathbb{C}^{ec} defined in equation (55) in Appendix D. Note that the resulting matrix is then non-symmetric. Note also that this angle discretization implies that k internal variables are introduced to keep track of the distribution of the backstress magnitude over the hemisphere.

The numerical algorithm to integrate in time these constitutive relations has its technical difficulties due to the risk of numerical fluctuation between slip and no-slip conditions in some orientations if an implicit update is chosen as described briefly in Appendix D. This is mainly because the stress point is initially close to the tip of the Coulomb cone in the space spanned by the normal stress and resolved shear stress (see Appendix F for further discussion). This problem, which is known in computational crystal plasticity [Raphanel et al., 2004], was solved by these authors by proposing a high-order explicit integration scheme. The same idea is proposed here, and the strain increment over the time step Δt is subdivided into m intervals to permit the application of an Adams-Bashforth scheme. The search for equilibrium at the end of the time step $t_{n+1} = t_n + \Delta t$ requires a numerical tangent ideally resulting from a consistent linearization of the update algorithm [Simo and Taylor, 1985] to warrant a quadratic rate of convergence. Still, it was proposed to simplify the linearization and to take for numerical tangent the sum of the continuum tangents at every intermediate step weighted by the integration scalars of the Adams-Bashforth scheme. Order m of 3 to 5 were tested, and the sub-quadratic convergence rate was indeed noticed. Order $m = 3$ is used for all numerical results presented here.

F Kinematic hardening

The two objectives of this Appendix are, first, to present the motivation for the introduction of kinematic hardening from a fracture mechanics point of view, and second to follow a cyclic loading for a single family of cracks with azimuthal symmetry. The stress loading is bi-axial and inspired by the state of stress close to the pore based on a linear elasticity response as presented in Appendix A with equation (36), setting the radius to the pore radius. The stress of state beyond the hydrostatic initial condition is indeed bi-axial:

$$\sigma_r = -p_f, \quad \sigma_\theta = \sigma_\varphi = -p_f - \Sigma \quad \text{with} \quad \Sigma = \frac{3(\sigma_H - p_f)}{2(1 - \phi)}, \quad (60)$$

keeping the fluid pressure constant.

623 F.1 Kinematic hardening and fracture mechanics

The effect of cracks under uniaxial loading has been demonstrated by many contributions since the seminal work of Walsh [1965]. One of the key ideas in that paper has been the stress conditions for the reverse slipping of the cracks at the start of the unloading phase: sliding to occur requires a reduction in the sum of the resolved shear stress plus the frictional shear stresses, $\Delta\tau + \Delta\tau_f$ twice as large as the maximum frictional stress τ_f^{max} :

$$\Delta\tau + \Delta\tau_f > 2\tau_f^{max}, \quad (61)$$

624 using Walsh [1965]'s notation. The resolved shear stress increment has the same definition as in this contribution
 625 (equation 6) while the frictional shear stress increment is $\mu(\Delta\sigma_n + \Delta p_f)$ in our setting. The maximum frictional stress
 626 is reached prior to the reverse loading and then reads $\mu(\sigma_n + \sigma_C + p_f)^{max}$.

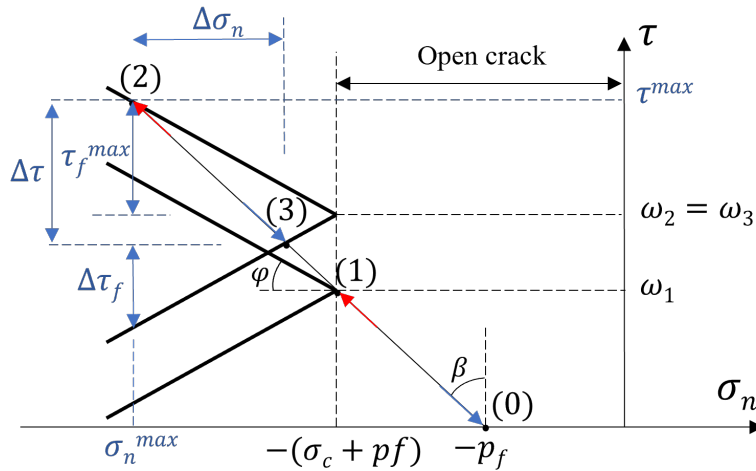


Figure (12) Evolution of the position of the elasticity domain in the stress space during a bi-axial loading cycle typical to the region close to the pore and for a crack family oriented by the first polar angle β . From the initial stress point (0) to (1), the crack is open and is closed up to (2) during loading. During the unloading phase, the crack sticks between (2) and (3). Reverse-slip occurs between (3) and up to the crack reopening at (1).

627 The explanation of this slip condition is not trivial, and some clarifications are now proposed using the arguments
 628 outlined in Andrieux et al. [1986] and based on the work of Muskhelishvili [1963]. For a 2D crack in an infinite medium,
 629 the normal stress on the crack lips is uniform and indeed equal to the normal stress based on the remote stress tensor,
 630 as defined in equation (4). As the crack closes, there is already a tangential displacement jump b_t , and the associated
 631 shear stress denoted ω equals this jump divided by the crack compliance γ introduced in equation (2). The resolved
 632 shear stress τ , based on the remote stress tensor, is also equal to ω at closure. The frictional forces to induce slip upon
 633 loading beyond closure are thus the normal stress and the difference between τ and ω , the latter being first defined by
 634 the elasticity problem up to closure. The yield criterion (6) is constructed based on these two forces and does remind
 635 us of a kinematic hardening plasticity law, although the back-stress, ω , has a life before crack closure. Its graphical
 636 representation in Figure 12 depicts the evolution in the stress space during a cyclic compression for a crack having for
 637 first polar angle β . In the loading phase, the crack remains open from the initial stress point (0) to point (1), after
 638 which it is closed. Note that at closure, the stress point is exactly at the apex of the Coulomb criterion. The crack
 639 sticks or slips if the condition $\varphi + \beta \geq \pi/2$ is met. If a slip occurs, it does so immediately after crack closure. The
 640 back stress keeps evolving based on the rate of tangential displacement jump across the crack surfaces divided by the
 641 elasticity compliance, equation (7). This displacement jump amplitude is governed by the consistency condition on the
 642 yield criterion, equations (8) and (9). The yield surface is thus continuously translated upward until the maximum load
 643 is reached at point (2) in Figure 12. In the subsequent unloading phase, the crack experiences sticking between points (2)
 644 and (3), and the back stress does not change since the tangential displacement jump is constant. Then reverse-slipping
 645 occurs between point (3) and the crack's reopening point (1). Note that the final slip during unloading is again at the
 646 apex of the yield criterion. The reasoning based on 2D elasticity solutions is applied to 3D in this contribution without
 647 further justification.

648 The rest of this Appendix is devoted to the evolution of the straining during the cyclic loading in a REV close to
 649 a spherical pore, as depicted above. The analysis is done for a single family of cracks with azimuthal symmetry to link
 650 with earlier work by David et al. [2012].

651 F.2 A single family with azimuthal symmetry

652 The stress-strain relation for a single family is still provided by equation (1) if the integrant is modified to include the
 653 distribution function $c^* \delta(\beta - \beta^*) / (2\pi \sin \beta)$ in which c^* is the crack density in the direction β^* orienting the crack family
 654 of interest and $\delta(\beta - \beta^*)$ the classical Dirac function. The strain-stress relation then simplifies to:

$$\underline{\dot{\epsilon}} = \mathbb{C} : (\underline{\dot{\sigma}} + \alpha \dot{p}_f \underline{\delta}) + \frac{c^*}{4l} \int_{\beta'=0}^{2\pi} \left(\dot{b}(\underline{n}^*) \otimes \underline{n}^* + \underline{n}^* \otimes \dot{b}(\underline{n}^*) \right) d\beta', \quad (62)$$

655 in which the normal \underline{n}^* is oriented by β^* and the second polar angle β' in the range $[0; 2\pi]$.

656 The loading due to the remote stress in (60) leads to straining $(\epsilon_r, 2\epsilon_\theta)$ with the open crack contribution in (62)
657 reading

$$\frac{c^* \gamma \pi}{l} \begin{bmatrix} \cos^2 \beta^* (1 - \frac{\nu}{2} \cos^2 \beta^*) & -\frac{\nu}{2} \cos^2 \beta^* \sin^2 \beta^* \\ -\frac{\nu}{2} \cos^2 \beta^* \sin^2 \beta^* & \sin^2 \beta^* (1 - \frac{\nu}{2} \sin^2 \beta^*) \end{bmatrix} \begin{Bmatrix} \dot{\sigma}_r + \dot{p}_f \\ \dot{\sigma}_\theta + \dot{p}_f \end{Bmatrix}, \quad (63)$$

658 using a matrix notation. The back-stress evolution before closure is dictated by the resolved shear stress $\underline{w} = \underline{\tau} =$
659 $(\sigma_r - \sigma_\theta) \cos \beta^* \sin \beta^* \underline{p}^*$ in which the vector \underline{p}^* is orthogonal to \underline{n}^* and defined in equation (56) of Appendix E for the
660 polar angles (β^*, β') . The contribution of (63) ceases once the crack family is closed, and this happens when the remote
661 loading is equal to $\sigma_H = 2(1 - \phi)\sigma_C / (3 \sin^2 \beta^*) + p_f$. In Figure 12, this loading path from the initial condition (0) brings
662 us to the stress point (1), which is at the tip of the Coulomb cone. In summary, at crack closure:

$$\begin{aligned} \tau_{(1)} = \omega_{(1)} = \Sigma_{(1)} \sin \beta^* \cos \beta^*, \quad \sigma_{n(1)} = -p_f - \Sigma_{(1)} \sin^2 \beta^* \quad \text{with} \quad \Sigma_{(1)} = \sigma_C \sin^{-2} \beta^*, \\ \epsilon_{\theta(1)} = -\frac{1}{2} \left(\frac{4G + 3\kappa}{9G\kappa} + \frac{c^* \gamma \pi}{l} \sin^2 \beta^* (1 - \frac{\nu}{2} \sin^2 \beta^*) \right) \Sigma_{(1)}. \end{aligned} \quad (64)$$

The case of interest is now $\varphi + \beta^* \geq \pi/2$ since slipping occurs immediately upon further loading after closure. From Appendix E, the crack family contribution to the straining is then:

$$\frac{c^* \gamma \pi}{l} \begin{bmatrix} \cos \beta^* (\sin \beta^* + \mu s \cos \beta^*) & -\sin \beta^* (\cos \beta^* - \mu s \sin \beta^*) \\ -\cos \beta^* (\sin \beta^* + \mu s \cos \beta^*) & \sin \beta^* (\cos \beta^* - \mu s \sin \beta^*) \end{bmatrix} \begin{Bmatrix} \dot{\sigma}_r + \dot{p}_f \\ \dot{\sigma}_\theta + \dot{p}_f \end{Bmatrix}, \quad (65)$$

663 with $s = 1$ during loading. The conditions at the end of this loading are then

$$\begin{aligned} \omega_{(2)} = \Sigma_{(2)} \sin \beta^* (\cos \beta^* + \mu \sin \beta^*) - \mu \Sigma_{(1)} \sin^2 \beta^*, \\ \epsilon_{\theta(2)} - \epsilon_{\theta(1)} = -\frac{1}{2} \left(\frac{4G + 3\kappa}{9G\kappa} + \frac{c^* \gamma \pi}{l} \sin \beta^* (\cos \beta^* - \mu \sin \beta^*) \right) (\Sigma_{(2)} - \Sigma_{(1)}), \end{aligned} \quad (66)$$

664 having used equation (9) to follow the evolution of the backstress. The unloading occurs with stick conditions, and the
665 conditions at the start of reverse sliding are:

$$\omega_{(3)} = \omega_{(2)}, \quad \Sigma_{(3)} = (\Sigma_{(2)} - 2\Sigma_{(1)}) \frac{\mu \sin \beta^*}{\cos \beta^* + \mu \sin \beta^*}, \quad \epsilon_{\theta(3)} - \epsilon_{\theta(2)} = -\frac{1}{2} \frac{4G + 3\kappa}{9G\kappa} (\Sigma_{(3)} - \Sigma_{(2)}). \quad (67)$$

666 Reverse slip occurs upon further unloading and implies that $s = -1$ in equation (65). It also means that the stress
667 conditions are back at point (1) at the final unloading, closing the hysteresis loop.

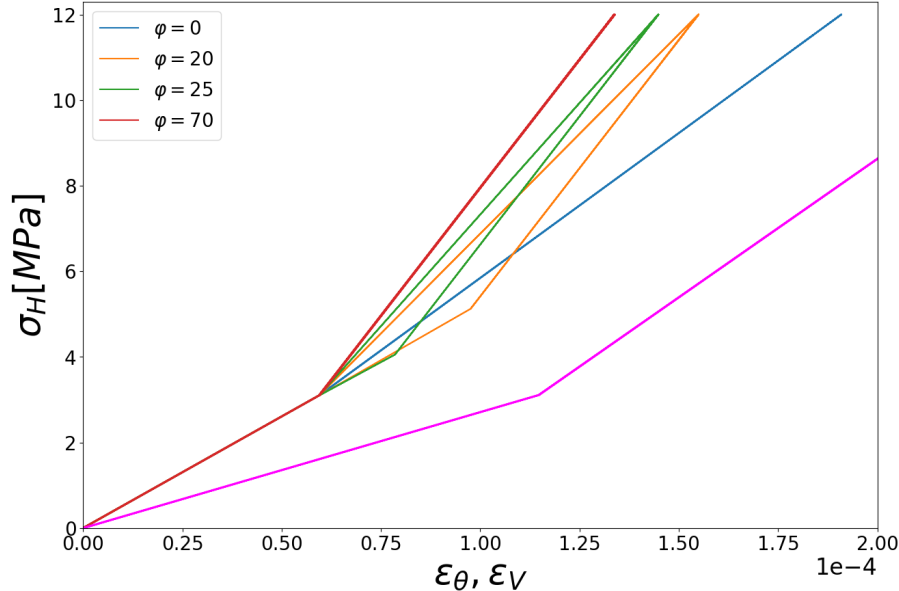


Figure (13) Remote stress σ_H versus hoop strain ϵ_θ and volumetric strain ϵ_V (magenta line) for a single family of cracks ($\beta^* = \pi/3$) at various crack's friction angles φ (in degrees) for dry conditions. The hysteresis in ϵ_θ is a function of the crack's friction, and the maximum effect is attained for an intermediate value of the friction angle. There is no hysteresis in volumetric strain by construction.

668 Figure 13 shows the deformation during the cyclic loading for various values of the frictional angle and under dry
669 conditions for the sake of simplicity. The cracks have the orientation angle $\beta^* = \pi/3$ so that the cracks are slipping unless
670 the friction angle φ is larger than $\pi/6$ (stick condition $\varphi + \beta^* \geq \pi/2$): the closure stress $\sigma_C = 4$ MPa, and the crack

671 density $c^* = 0.6$. The porosity of the specimen is $\phi = 0.125$, while the matrix elastic properties are set to ($E = 95.46$
672 GPa, $\nu = 0.07$ corresponding to quartz). The loading cycle consists of a loading phase, with σ_H varying from 0 MPa
673 to 12 MPa, and an unloading back to initial conditions. The four stress-strain curves σ_H vs ϵ_θ are multi-linear and
674 characterised by four values for the slope E_θ defined with:

$$\begin{aligned} \dot{\sigma}_H &= -E_\theta \dot{\epsilon}_\theta \quad \text{with} & (68) \\ \frac{1}{E_\theta} &= \frac{4G + 3\kappa}{12G\kappa(1 - \phi)} \quad \text{closed and sticking cracks,} \\ \frac{1}{E_\theta} &= \frac{4G + 3\kappa}{12G\kappa(1 - \phi)} + \frac{3c^*\gamma\pi}{4l(1 - \phi)} \frac{\sin\beta^*}{\cos\varphi} \cos(\beta^* + s\varphi) \quad \text{closed and slipping cracks,} \\ \frac{1}{E_\theta} &= \frac{4G + 3\kappa}{12G\kappa(1 - \phi)} + \frac{3c^*\gamma\pi}{4l(1 - \phi)} \sin^2\beta^* \left(1 - \frac{\nu}{2} \sin^2\beta^*\right) \quad \text{open cracks.} \end{aligned}$$

675 Crack closure occurs at σ_H , approximately equal to 3.1 MPa, before which the stress-strain curve is independent
676 of friction. If there is no friction ($\varphi = 0$), the cracks slip since $\varphi + \beta^* \leq \pi/2$. In addition, E_θ is the same during the
677 loading and unloading stages as seen in equation (68)c ($\varphi = 0$). There is also no sticking phase since the yield surface
678 cone is closed, and reverse slipping happens at the very start of the unloading, Figure 12. On the contrary, if $\varphi = 20^\circ$
679 and $\varphi = 25^\circ$ the cracks first slip in the loading stage since $\varphi + \beta^* \leq \pi/2$ but stick at the beginning of the unloading.
680 The sticking modulus E_θ is the same for both values of φ as it is independent of friction. Also, the sticking phase is
681 longer at $\varphi = 25^\circ$ compared to $\varphi = 20^\circ$ because, as shown in Figure 12, in the former, the yield surface cone is larger
682 than in the latter, meaning that a greater decrease of stress is required to reverse slip. Note that, in the slipping phases,
683 E_θ loading is greater at $\varphi = 25^\circ$ than at $\varphi = 20^\circ$, whereas it is the opposite during the unloading, in agreement with
684 equation (68)c. Finally, if $\varphi = 70^\circ$, the cracks always stick since $\varphi + \beta^* \geq \pi/2$.

685 One last point to note is that no matter the value of the crack's friction, the volumetric strain versus the stress
686 curve shows no hysteresis (magenta line). This is because crack slipping induces no volumetric change within the REV.
687 Its modulus κ^* is thus constant regardless of the crack slipping unless more complex geometries such as wing cracks
688 are accounted for. However, crack slipping reduces the equivalent shear modulus G^* of the REV and thus does lead to
689 hysteresis in the volumetric macro response of the assemblage as revealed by the classical relation (26).

690 G Spherical Assembly effective properties for slipping cracks

691 The objective is to derive an analytical solution for the bulk modulus, Biot's coefficient and the pore volume fraction rate
692 of the assemblage if all cracks are closed and slipping. For closed and sticking cracks and for open cracks, the solution is
693 presented in the main text, relying on Appendices A and B. The analytical expression of the bulk modulus in the general
694 case of a distribution of cracks either open, closed, and sticking or slipping is challenging to derive since the material
695 moduli are heterogeneous within the shell. There is a particular case for which homogeneity is conserved in terms of
696 moduli, and it corresponds to a distribution of closed and slipping cracks at all radii of the hollow sphere.

697 The starting point is again the definition of the stress-strain relation in equation (1) with the crack strain rate defined
698 in (59) with β_c set to zero since all cracks are closed. The quadrature is exact, and the strain-stress rates relation is
699 simplified to:

$$\begin{Bmatrix} \dot{\epsilon}_r \\ 2\dot{\epsilon}_\theta \end{Bmatrix} = \frac{1}{9G\kappa} \begin{bmatrix} G + 3\kappa & 2G - 3\kappa \\ 2G - 3\kappa & 4G + 3\kappa \end{bmatrix} \begin{Bmatrix} \dot{\sigma}_r + \alpha\dot{p}_f \\ \dot{\sigma}_\theta + \alpha\dot{p}_f \end{Bmatrix} + \frac{4c\gamma\pi^2}{15l} \begin{bmatrix} 1 + \mu s & -(1 - \frac{3}{2}\mu s) \\ -(1 + \mu s) & 1 - \frac{3}{2}\mu s \end{bmatrix} \begin{Bmatrix} \dot{\sigma}_r + \dot{p}_f \\ \dot{\sigma}_\theta + \dot{p}_f \end{Bmatrix}. \quad (69)$$

700 This system of equations is now inverted to express the stress rates in relation to the strain and the pressure rates:

$$\begin{Bmatrix} \dot{\sigma}_r \\ \dot{\sigma}_\theta \end{Bmatrix} = \frac{1}{D} \begin{bmatrix} 4G + 3\kappa + 9G\kappa\Gamma(1 - \frac{3}{2}\mu s) & -2G + 3\kappa + 9G\kappa\Gamma(1 - \frac{3}{2}\mu s) \\ -2G + 3\kappa + 9G\kappa\Gamma(1 + \mu s) & G + 3\kappa + 9G\kappa\Gamma(1 + \mu s) \end{bmatrix} \left(\begin{Bmatrix} \dot{\epsilon}_r \\ 2\dot{\epsilon}_\theta \end{Bmatrix} - \begin{Bmatrix} \frac{\alpha}{3\kappa} + \Gamma\frac{5}{2}\mu s \\ \frac{2\alpha}{3\kappa} - \Gamma\frac{5}{2}\mu s \end{Bmatrix} \dot{p}_f \right),$$

with $D = 3[1 + \Gamma G(3 + \frac{1}{2}\mu s)]$ and $\Gamma = \frac{4c\gamma\pi^2}{15l}$. (70)

701 Note that the matrix component on the right-hand side of this equation is denoted A_{ij}/D with $i, j = r$ or θ in what
702 follows.

703 Introduce these expressions into the equilibrium equations (32) and obtain:

$$\begin{aligned} [4G + 3\kappa + 9G\kappa\Gamma(1 - \frac{3}{2}\mu s)]r \frac{\partial^2 \dot{u}}{\partial r^2} + 2[4G + 3\kappa + 9G\kappa\Gamma(1 - 4\mu s)] \frac{\partial \dot{u}}{\partial r} & (71) \\ -2[4G + 3\kappa + 9G\kappa\Gamma(1 + \frac{7}{2}\mu s)] \frac{\dot{u}}{r} = 45G\Gamma\mu s(1 - \alpha)\dot{p}_f. & \end{aligned}$$

The homogeneous part of this differential equation is a second-order Cauchy-Euler equation, which is solved with the
trial function $(r/R_S)^m$, and the exponent m is the solution of the second-order polynomial

$$m^2 + m \frac{4G + 3\kappa + 9G\kappa\Gamma(1 - \frac{13}{2}\mu s)}{4G + 3\kappa + 9G\kappa\Gamma(1 - \frac{3}{2}\mu s)} - 2 \frac{4G + 3\kappa + 9G\kappa\Gamma(1 + \frac{7}{2}\mu s)}{4G + 3\kappa + 9G\kappa\Gamma(1 - \frac{3}{2}\mu s)} = 0. \quad (72)$$

The unexpected finding is that one of the two roots of this polynomial is the scalar -2 for all friction values so that the two roots read:

$$m_1 = \frac{4G + 3\kappa + 9G\kappa\Gamma(1 + \frac{7}{2}\mu_s)}{4G + 3\kappa + 9G\kappa\Gamma(1 - \frac{3}{2}\mu_s)}, \quad m_2 = -2. \quad (73)$$

Note that the first root is close to 1, and the set (1, -2) corresponds to the two powers of the displacement polynomial found for an isotropic, elastic solid, as seen in Appendix A. The final expression for the displacement rate is:

$$\dot{u}(r) = C_1 R_S \left(\frac{r}{R_S}\right)^{m_1} + C_2 R_S \left(\frac{r}{R_S}\right)^{-2} - r \frac{1}{3} (1 - \alpha) \frac{\dot{p}_f}{\kappa}, \quad (74)$$

704 for two dimensionless constants C_1 and C_2 which are obtained from the stress-boundary conditions as follows.

The first of the three steps to find these constants is to express the stress rate in equation (70) in terms of the two unknowns:

$$\begin{Bmatrix} \dot{\sigma}_r + \dot{p}_f \\ \dot{\sigma}_\theta + \dot{p}_f \end{Bmatrix} = \frac{C_1}{D} \left(\frac{r}{R_S}\right)^{m_1-1} \begin{Bmatrix} A_{rr}m_1 + 2A_{r\theta} \\ A_{\theta r}m_1 + 2A_{\theta\theta} \end{Bmatrix} + \frac{2C_2}{D} \left(\frac{r}{R_S}\right)^{-3} \begin{Bmatrix} -A_{rr} + A_{r\theta} \\ -A_{\theta r} + A_{\theta\theta} \end{Bmatrix}. \quad (75)$$

The second step sees the application of the stress boundary conditions $\dot{\sigma}_r|_{R_P} = -\dot{p}_f$ and $\dot{\sigma}_r|_{R_S} = -\dot{\sigma}_H$ at the pore radius and the external radius, respectively. These two conditions combined with the first equation in (75) provide a system of two equations for the unknown scalars:

$$\begin{Bmatrix} 0 \\ -\dot{\sigma}_H + \dot{p}_f \end{Bmatrix} = \frac{1}{D} \begin{bmatrix} (A_{rr}m_1 + 2A_{r\theta})\phi^{\frac{1}{3}(m_1-1)} & 2(-A_{rr} + A_{r\theta})\phi^{-1} \\ A_{rr}m_1 + 2A_{r\theta} & 2(-A_{rr} + A_{r\theta}) \end{bmatrix} \begin{Bmatrix} C_1 \\ C_2 \end{Bmatrix}. \quad (76)$$

705 The third and final step consists of inverting this system to determine the two constants:

$$\begin{Bmatrix} C_1 \\ C_2 \end{Bmatrix} = (-\dot{\sigma}_H + \dot{p}_f) \begin{Bmatrix} \tilde{C}_1 \\ \tilde{C}_2 \end{Bmatrix} \quad \text{with} \quad \begin{Bmatrix} \tilde{C}_1 \\ \tilde{C}_2 \end{Bmatrix} = \frac{D}{D'} \begin{Bmatrix} 2(A_{rr} - A_{r\theta})\phi^{-1} \\ (A_{rr}m_1 + 2A_{r\theta})\phi^{\frac{1}{3}(m_1-1)} \end{Bmatrix} \quad (77)$$

and $D' = -2(A_{rr}m_1 + 2A_{r\theta})(A_{rr} - A_{r\theta})(\phi^{\frac{1}{3}(m_1-1)} - \phi^{-1})$,

706 having introduced two constants \tilde{C}_1 and \tilde{C}_2 which have dimension of one over stress.

707 The solution for the displacement being determined, the rate of volume change $\dot{\theta} = 3\dot{u}(R_S)/R_S$ is now expressed in
708 terms of the pressure and hydrostatic rate of changes thanks to (74) and (77) providing the final expression:

$$\dot{\sigma}_H = -\bar{\kappa}_s \dot{\theta} + \bar{\alpha}_s \dot{p}_f \quad (78)$$

with $\bar{\kappa}_s = \frac{1}{3(\tilde{C}_1 + \tilde{C}_2)}$ and $\bar{\alpha}_s = 1 - (1 - \alpha) \frac{\bar{\kappa}_s}{\kappa}$.

709 in which the effective bulk modulus $\bar{\kappa}_s$ and the effective Biot's coefficient $\bar{\alpha}_s$ are introduced. Note again that these two
710 material parameters are defined for all cracks of the spherical assembly being in slip condition, as marked by the letter
711 s in subscript.

This solution for the effective properties of the assemblage with all cracks slipping, although analytical, requires a numerical implementation, which can be checked in the case of zero friction. In that instance, the solutions for the two exponents m_1 and m_2 in equation (72) are 1 and -2, as already pointed out above. The displacement has indeed the same structure as in (33) of Appendix A for an isotropic elastic solid. Inspection of the system (70) with $\mu = 0$ confirms this interpretation and reveals that the effective moduli and coefficient are:

$$\kappa^* = \kappa, \quad G^* = G/(1 + 3G\Gamma), \quad \alpha^* = \alpha \quad \text{and} \quad \bar{\kappa}_s = \kappa \frac{1 - \phi}{1 + \frac{3\kappa}{4G}(1 + 3G\Gamma)\phi}. \quad (79)$$

712 Note that the results for the particular case of zero friction are easily extended to the case of a constrained fluid volume
713 using (20).

714 The rest of this Appendix is devoted to the pore volume fraction, the volume of fluid within the porous medium
715 normalized by the volume of the spherical assembly. The non-linear evolution of this pore volume fraction, accounting
716 for the dead volume of the experiment, is discussed in detail in Section 2.2. The two objectives are first to concentrate on
717 the rate form adopted for the effective properties of the spherical assemblage summarized by equation (24) and second,
718 to derive expressions for the Biot's coefficient and the storage coefficient based thus on the second equation in (23). This
719 is, of course, a check that the general structure of the constitutive relations discussed in section 2.3.1 is valid.

720 The volume of fluid within the assemblage is due to the cracked matrix composing the shell and the central pore.
721 Since all cracks are assumed closed, the matrix pore volume change is still given by equation (10) with $\dot{\epsilon}_{vC}$ set to zero.
722 The pore volume fraction of the matrix is thus:

$$\dot{v} = \alpha C_1 (2 + m_1) \left(\frac{r}{R_S}\right)^{m_1-1} + \dot{p}_f (R_{pM} - \alpha(1 - \alpha) \frac{1}{\kappa}), \quad (80)$$

723 having made use of the displacement in (74) to deduce the local volume change. Integrate this contribution over the
724 shell and normalize by the volume of the assemblage to obtain the contribution to the assemblage pore volume change:

$$\alpha C_1 3(1 - \phi^{\frac{m_1+2}{3}}) + \dot{p}_f (R_{pM} - \alpha(1 - \alpha)\frac{1}{\kappa})(1 - \phi). \quad (81)$$

The second contribution is due to the central pore, and its contribution to the assemblage after normalization is $\phi \dot{u}(R_P)/R_P$ or based on the displacement field in (74):

$$3[C_1 \phi^{\frac{m_1+2}{3}} + C_2] - \phi(1 - \alpha)\frac{\dot{p}_f}{\kappa}. \quad (82)$$

725 The sum of these two contributions (81 and 82) is the pore volume fraction rate of the assemblage. It remains to replace
 726 the constants C_1 and C_2 by the expressions in (77), which are functions of the remote stress and fluid pressure rate. The
 727 former is eliminated thanks to the first equation in (24) so that the effective parameters are finally obtained:

$$\begin{aligned} \bar{\alpha}_s &= \frac{\tilde{C}_1[\phi^{\frac{m_1+2}{3}} + \alpha(1 - \phi^{\frac{m_1+2}{3}})] + \tilde{C}_2}{\tilde{C}_1 + \tilde{C}_2}, \\ \bar{R}_{ps} &= R_{pM}(1 - \phi) - \frac{1 - \alpha}{\kappa}(\phi + \alpha(1 - \phi)) \\ &\quad + 3(1 - \bar{\alpha}_s) \left(\tilde{C}_1[\alpha(1 - \phi^{\frac{m_1+2}{3}}) + \phi^{\frac{m_1+2}{3}}] + \tilde{C}_2 \right). \end{aligned} \quad (83)$$

728 The comparison between (78) and the first equation above is now necessary to confirm the symmetry argument discussed
 729 in section 2.3.1. Introduce the definition of $\bar{\kappa}_s$ in (78) to eliminate the sum $\tilde{C}_1 + \tilde{C}_2$ while making sure that only \tilde{C}_1
 730 remains in the expression. Use the definition of that constant in (77) and conclude that the two expressions (78) and
 731 (83) for Biot's coefficient are indeed equivalent. A non-trivial check of our derivation but also a confirmation, albeit not
 732 a proof of the statement made in section 2.3.1.

733 References

- 734 V. Aleshin and K. Van Den Abeele. Microcontact-based theory for acoustics in microdamaged materials. *Journal of the*
735 *Mechanics and Physics of Solids*, 55(2):366–390, 2007.
- 736 S. Andrieux, Y. Bamberger, and J.-J. Marigo. A model of micro-cracked material for concretes and rocks. *Journal de*
737 *Mécanique Théorique et Appliquée*, 5(3):471–513, 1986.
- 738 Y. Benveniste. The effective mechanical behaviour of composite materials with imperfect contact between the con-
739 stituents. *Mechanics of Materials*, 4(2):197–208, 1985. ISSN 0167-6636. doi: [https://doi.org/10.1016/0167-6636\(85\)](https://doi.org/10.1016/0167-6636(85)90016-X)
740 90016-X.
- 741 J. V. M. Borgomano, L. Pimienta, J. Fortin, and Y. Guéguen. Dispersion and attenuation measurements of the elastic
742 moduli of a dual-porosity limestone. *Journal of Geophysical Research: Solid Earth*, 122(4):2690–2711, 2017.
- 743 S. Chapman, J. Fortin, A. Gallagher, and J. V. Borgomano. Strain amplitude dependent transition from dynamic to
744 static bulk modulus in rocks with and without pre-existing cracks. *Rock Mechanics and Rock Engineering*, pages 1–18,
745 2023.
- 746 R. Christensen and K. Lo. Solutions for effective shear properties in three phase sphere and cylinder models. *Journal of*
747 *the Mechanics and Physics of Solids*, 27(4):315–330, 1979.
- 748 R. M. Christensen. A critical evaluation for a class of micro-mechanics models. *Journal of the Mechanics and Physics*
749 *of Solids*, 38(3):379–404, 1990. ISSN 0022-5096.
- 750 E. C. David, N. Brantut, A. Schubnel, and R. W. Zimmerman. Sliding crack model for nonlinearity and hysteresis in
751 the uniaxial stress–strain curve of rock. *International Journal of Rock Mechanics and Mining Sciences*, 52:9–17, 2012.
- 752 Z. Hashin. The elastic moduli of heterogeneous materials. *Journal of Applied Mechanics*, 29:143–150, 1962.
- 753 E. Hervé and A. Zaoui. n-layered inclusion-based micromechanical modelling. *International Journal of Engineering*
754 *Science*, 31(1):1–10, 1993.
- 755 J. C. Jaeger, N. G. Cook, and R. W. Zimmerman. *Fundamentals of rock mechanics*. John Wiley & Sons, 2009.
- 756 D. Jizba and A. Nur. Static and dynamic properties of sandstones. In *EAGE/SEG Research Workshop 1990*, pages
757 cp–53. European Association of Geoscientists & Engineers, 1990.
- 758 M. L. Kachanov. A microcrack model of rock inelasticity part I: Frictional sliding on microcracks. *Mechanics of Materials*,
759 1(1):19–27, 1982.
- 760 M. L. Kachanov. Effective Elastic Properties of Cracked Solids: Critical Review of Some Basic Concepts. *Applied*
761 *Mechanics Reviews*, 45(8):304–335, 08 1992.
- 762 L. Knopoff. Q. *Reviews of Geophysics*, 2(4):625–660, 1964.
- 763 R. Martin III and R. Haupt. Static and dynamic elastic moduli in granite: The effect of strain amplitude. In *ARMA*
764 *North America Rock Mechanics Symposium*, pages ARMA–1994–0473, 1994.
- 765 N. Muskhelishvili. Some basic problems of the mathematical theory of elasticity. *Noordhoff, Groningen*, 17404(6.2):1,
766 1963.
- 767 R. J. O’Connell and B. Budiansky. Measures of dissipation in viscoelastic media. *Geophysical Research Letters*, 5(1):
768 5–8, 1978.
- 769 M.-J. Pan, D. Green, and J. Hellmann. Influence of interfacial microcracks on the elastic properties of composites.
770 *Journal of materials science*, 31:3179–3184, 1996.
- 771 L. Pimienta, J. Fortin, and Y. Guéguen. Bulk modulus dispersion and attenuation in sandstones. *Geophysics*, 80(2):
772 D111–D127, 2015.
- 773 W. Prager. The theory of plasticity: A survey of recent achievements. *Proceedings of the Institution of Mechanical*
774 *Engineers*, 169(1):41–57, 1955.
- 775 J. L. Raphanel, G. Ravichandran, and Y. M. Leroy. Three-dimensional rate-dependent crystal plasticity based on Runge–
776 Kutta algorithms for update and consistent linearization. *International Journal of Solids and Structures*, 41(22-23):
777 5995–6021, 2004.
- 778 J. R. Rice. Pore pressure effects in inelastic constitutive relations for fissured rock masses. In *Advances in Civil*
779 *Engineering Through Engineering Mechanics (Proceedings of 2nd ASCE Engineering Mechanics Division Specialty*
780 *Conference, Raleigh, N.C.*, pages 295–297, 1977.

- 781 J. R. Rice and M. P. Cleary. Some basic stress diffusion solutions for fluid-saturated elastic porous media with compressible
782 constituents. *Reviews of Geophysics*, 14(2):227–241, 1976.
- 783 J. C. Simo and R. L. Taylor. Consistent tangent operators for rate-independent elastoplasticity. *Computer Methods in*
784 *Applied Mechanics and Engineering*, 48(1):101–118, 1985.
- 785 N. Tisato and C. Madonna. Attenuation at low seismic frequencies in partially saturated rocks: Measurements and
786 description of a new apparatus. *Journal of Applied Geophysics*, 86:44–53, 2012.
- 787 G. F. Vasquez, M. J. Morschbacher, and J. C. R. Justen. Experimental efforts to access 4d feasibility and interpretation
788 issues of brazilian presalt carbonate reservoirs. *Interpretation*, 7(4):SH1–SH18, 2019.
- 789 J. B. Walsh. The effect of cracks on the uniaxial elastic compression of rocks. *Journal of Geophysical Research*, 70(2):
790 399–411, 1965.
- 791 L. Wang, E. Rybacki, A. Bonnelye, M. Bohnhoff, and G. Dresen. Experimental investigation on static and dynamic bulk
792 moduli of dry and fluid-saturated porous sandstones. *Rock Mechanics and Rock Engineering*, 54(1):129–148, 2021.
- 793 R. Zimmerman. Coupling in poroelasticity and thermoelasticity. *International Journal of Rock Mechanics and Mining*
794 *Sciences*, 37:79–87, 2000.